Published in final edited form as:

Cell Rep. 2022 April 26; 39(4): 110737. doi:10.1016/j.celrep.2022.110737.

Structural basis of TRPV5 regulation by physiological and pathophysiological modulators

Edwin C. Fluck[1,2], **Aysenur Torun Yazici**[3], **Tibor Rohacs**[3], **Vera Y. Moiseenkova-Bell**[1,4,*]

[1]Department of Systems Pharmacology and Translational Therapeutics, Perelman School of Medicine, University of Pennsylvania, Philadelphia, PA 19104, USA

[2]Biochemistry and Molecular Biophysics Graduate Group, Perelman School of Medicine, University of Pennsylvania, Philadelphia, PA 19104, USA

[3]Department of Pharmacology, Physiology and Neuroscience, New Jersey Medical School, Rutgers University, Newark, NJ 07103, USA

[4]Lead contact

SUMMARY

Transient receptor potential vanilloid 5 (TRPV5) is a kidney-specific Ca^{2+}-selective ion channel that plays a key role in Ca^{2+} homeostasis. The basal activity of TRPV5 is balanced through activation by phosphatidylinositol 4,5-bisphosphate ($PI(4,5)P_2$) and inhibition by Ca^{2+}-bound calmodulin (CaM). Parathyroid hormone (PTH), the key extrinsic regulator of Ca^{2+} homeostasis, increases the activity of TRPV5 via protein kinase A (PKA)-mediated phosphorylation. Metabolic acidosis leads to reduced TRPV5 activity independent of PTH, causing hypercalciuria. Using cryoelectron microscopy (cryo-EM), we show that low pH inhibits TRPV5 by precluding $PI(4,5)P_2$ activation. We capture intermediate conformations at low pH, revealing a transition from open to closed state. In addition, we demonstrate that $PI(4,5)P_2$ is the primary modulator of channel gating, yet PKA controls TRPV5 activity by preventing CaM binding and channel inactivation. Our data provide detailed molecular mechanisms for regulation of TRPV5 by two key extrinsic modulators, low pH and PKA.

Graphical Abstract

*Correspondence: vmb@pennmedicine.upenn.edu.

AUTHOR CONTRIBUTIONS

Conceptualization, E.C.F. and V.Y.M.-B.; methodology, E.C.F. and V.Y.M.-B.; validation, E.C.F. and A.T.Y.; formal analysis, E.C.F. and A.T.Y.; investigation, E.C.F. and A.T.Y.; writing – original draft, E.C.F. and V.Y.M.-B., writing – review & editing, E.C.F., A.T.Y., T.R., and V.Y.M.-B.; visualization, E.C.F. and A.T.Y.; funding acquisition, T.R. and V.Y.M.-B.; supervision, T.R. and V.Y.M.-B.

SUPPLEMENTAL INFORMATION

Supplemental information can be found online at https://doi.org/10.1016/j.celrep.2022.110737.

DECLARATION OF INTERESTS

The authors declare no competing interests.

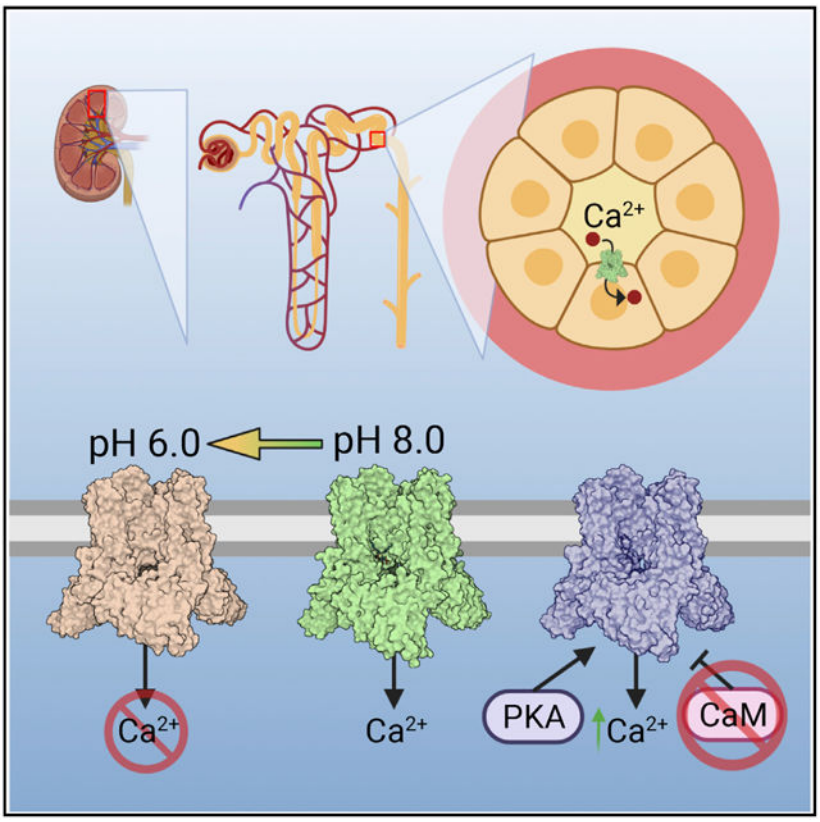

In brief

Fluck et al. investigate how the activity of TRPV5 is decreased by acidic pH environments and increased by PKA phosphorylation. Combining cryo-EM and electrophysiology, their results show that acidic environments cause channel closing and loss of PI(4,5)P_2 binding, whereas PKA phosphorylation disrupts CaM inactivation.

INTRODUCTION

Calcium homeostasis is essential for survival and is accomplished through the coordination of functions in the intestine, bone, and kidney (Frick and Bushinsky, 2003; van de Graaf et al., 2007). In the kidney, transient receptor potential vanilloid 5 (TRPV5) is the key regulator of calcium homeostasis (Hoenderop et al., 2005). It functions by reabsorbing calcium from the tubular fluid and facilitating its transport back into the circulation (van de Graaf et al., 2007; van Goor et al., 2017; Zhou and Greka, 2016). Mice lacking TRPV5 display hypercalciuria and disruptions to bones (Hoenderop et al., 2003). Furthermore, loss-of-function mutations of TRPV5 in humans are associated with kidney stones (Oddsson et al., 2015; Wang et al., 2017). Parathyroid hormone (PTH), the key regulator of Ca^{2+} homeostasis, increases Ca^{2+} reabsorption in the kidney by increasing TRPV5 activity via protein kinase A (PKA)-mediated phosphorylation (de Groot et al., 2008, 2009, 2011; van Abel et al., 2005).

Chronic metabolic acidosis is a condition that leads to increased calcium excretion in the urine (Nijenhuis et al., 2006). Urine pH can reach as low as pH 4.4 in some conditions, and low pH has been shown to inhibit the transport of calcium in the distal nephron (Bindels et al., 1994; Hoenderop et al., 2002). TRPV5 is directly inhibited by low pH, and the channel was proposed to contain both intra- and extracellular titratable pH sensors, Lys607 and Glu522 (Cha et al., 2007; Hoenderop et al., 1999; Yeh et al., 2003, 2005). It has been shown that low intracellular pH decreases the open probability of the channel (P_o) (Cha et al., 2007). While functional studies have revealed aspects of TRPV5 modulation by pH (Cha et al., 2007; Hoenderop et al., 1999; Yeh et al., 2003, 2005), limited information can be deduced about the structural mechanisms of the pH regulation of TRPV5.

TRPV5 shows constitutive activity, which is maintained by activation of its endogenous co-factor phosphatidylinositol 4,5-bisphosphate ($PI(4,5)P_2$) (Lee et al., 2005). TRPV5 also undergoes Ca^{2+}-induced inactivation, which is mediated by calmodulin (CaM) binding to the channel (de Groot et al., 2011). The precise balance between $PI(4,5)P_2$ activation and CaM inhibition determines the basal activity of the channel (Cao et al., 2013; van der Wijst et al., 2019). Recently, TRPV5 structural studies in the presence of CaM and $PI(4,5)P_2$ revealed how this channel's constitutive activity is accomplished. $PI(4,5)P_2$ binding is coordinated by the four positively charged residues located between the N linker (Arg302, Arg305), the S4–S5 linker (Lys484), and the S6 helix (Arg584) of the channel, and it induces TRPV5 conformational rearrangements to dilate the pore in order to open the channel (Hughes et al., 2018b). Calcium-activated CaM binds to the distal C terminus (residues His699–Thr709) of the channel and sterically blocks the ion-conducting pore at Trp583 through a cation-π interaction with Lys116 on the C lobe of CaM (Dang et al., 2019; Hughes et al., 2018b). However, the structural basis of the regulation of the channel by extrinsic physiological and pathophysiological regulators such as PKA and low pH, and their relationship to $PI(4,5)P_2$ and CaM, has not been studied.

Here, we used cryoelectron microscopy (cryo-EM) to gain structural insights into the mechanism of TRPV5 modulation by low pH and PKA and their relationship to the intrinsic regulators $PI(4,5)P_2$ and CaM. Our results show that low pH precludes TRPV5 interaction with $PI(4,5)P_2$ and reveal unique synergetic effects of pH and the lipid co-factor on channel gating. Moreover, our results suggest that PKA phosphorylation is another modulator of channel activity that interplays with $PI(4,5)P_2$ and CaM modulation. These data provide understanding of the TRPV5 regulation in the kidney by two key physiological and pathophysiological regulators, which may pave the road to development of better therapeutics for kidney stone disease.

RESULTS

TRPV5 pH modulation

To understand how TRPV5 is modulated by pH, first we measured TRPV5 activity in *Xenopus* oocytes using two-electrode voltage clamp (TEVC) recordings. We measured inwardly rectifying monovalent TRPV5 currents upon application of solutions with different pH values. Figure 1A shows that lower extracellular pH decreases TRPV5 current

amplitudes, which is consistent with earlier whole-cell patch-clamp experiments in CHO cells (Yeh et al., 2003).

Following our electrophysiological results, we investigated the effect of low pH on TRPV5 at the structural level using high-resolution cryo-EM. Full-length rabbit TRPV5 was reconstituted into nanodiscs, and the structure of the apo TRPV5 at pH 8.0 ($TRPV5_{pH8}$) was determined using cryoSPARC at 3.2 Å resolution (Figures 1B, 1C, and S1; Table 1). To determine TRPV5 structures at lower pH, TRPV5 was first reconstituted into nanodiscs at pH 8.0 and then the buffer pH was adjusted to pH 5.0 or to pH 6.0, followed by 5 min of incubation before the sample was frozen. Data were also processed using cryoSPARC and produced the $TRPV5_{pH6}$ structure at 3 Å resolution and $TRPV5_{pH5}$ structure at 3.7 Å resolution (Figures 1B, 1C, and S1; Table 1). The domain architectures of each of these newly solved TRPV5 structures in nanodiscs were similar to previously reported TRPV5 structures (Dang et al., 2019; Hughes et al., 2018a, 2018b, 2019) (Figure S2).

To compare these three new TRPV5 structures ($TRPV5_{pH8}$, $TRPV5_{pH6}$, $TRPV5_{pH5}$), we aligned them on the tetrameric pore (Lys490–Phe512 and Phe553–Ala586) of each channel. Upon comparison (Figures 1B–1G and S3A), we noted that $TRPV5_{pH6}$ and $TRPV5_{pH5}$ adopted a different conformation from $TRPV5_{pH8}$ (Figures 1B–1G). While the pore radii at Ile575 of $TRPV5_{pH6}$ (1.2 Å) and $TRPV5_{pH5}$ (0.7 Å) were comparable to that of $TRPV5_{pH8}$ (0.9 Å) (Figure S3A), in both low-pH structures one difference could be seen clearly in the new position of Trp583 at the bottom of the channel pore that narrowed the ion-permeation pathway (Figures 1B, 1C, and S3A). In addition to changes observed in the pore domain between $TRPV5_{pH8}$, $TRPV5_{pH6}$, and $TRPV5_{pH5}$ (Figures 1B and 1C), we noted that the ankyrin repeat domain (ARD) adopted a slightly different conformation in the $TRPV5_{pH6}$ and $TRPV5_{pH5}$ structures. At low pH, the ARDs of TRPV5 moved upward by 2.2 Å toward the transmembrane domain (TMD) compared with $TRPV5_{pH8}$ (Figure 1F) and rotated slightly (Figure 1G). These conformational changes in the channel seem to be initiated by the formation of a salt-bridge network near the proposed intracellular pH sensor Lys607 (Figures 1D, S4A, and S4B). A salt bridge forms between amino acid residues of opposite charges via an electrostatic interaction within 4 Å of distance (Donald et al., 2011). Particularly, in the $TRPV5_{pH5}$ and $TRPV5_{pH6}$ structures, Arg606 and Lys607 both interact with Asp406 and form two salt bridges, which could not be observed in the $TRPV5_{pH8}$ structure (Figures 1D, S4A, and S4B). Moreover, the formation of the salt bridge between Arg409 and Glu294 may also stabilize these newly observed states at low pH (Figures 1D, S4A, and S4B). Together, the formation of these three salt bridges between TRP helix, S2–S3 linker, and N linker locked the channel into this new low-pH state (Figure 1). Lowering the pH did not have an effect on the proposed extracellular pH sensor Glu522 (Figure 1E). While we identified the molecular mechanism of the pH effect on the proposed intracellular pH sensor near Lys607 in the channel, the experiments could not demonstrate how pH exactly inhibited the channel, as all three structures are essentially in a closed state.

We hypothesized that since the key endogenous activator of TRPV5 is $PI(4,5)P_2$ (Lee et al., 2005), its addition to nanodisc-reconstituted TRPV5 and lowering of the pH would allow us to better recapitulate the native environment of TRPV5 and the effect of pH on channel gating. To investigate this effect, we determined the structure of TRPV5 at pH 6.0 in the

presence of PI(4,5)P_2 under two conditions (Figures 2 and S5; Table 1). We chose to pursue pH 6.0 for these studies, since sample quality significantly diminished at pH 5.0. Under condition 1, nanodisc-reconstituted TRPV5 was incubated with PI(4,5)P_2 at pH 8.0 first, as we reported previously (Hughes et al., 2018b), and then the sample pH was adjusted to pH 6.0 for 5 min before freezing. We determined two structures from condition 1: the first structure at 2.7 Å resolution contained a clear PI(4,5)P_2 density; therefore we named this structure TRPV5$_{pH6+PIP2-state1}$ (Figures 2B, 2G, 3B, 3G, 3K, 3O, and S5). A second structure at 2.8 Å resolution did not contain a PI(4,5)P_2 density, and we named this structure TRPV5$_{pH6-state2}$ (Figures 2C, 2H, and S5). These two structures had similar numbers of particles (Figures 2 and S5; Table 1).

Under condition 2, the sample was first adjusted to pH 6.0 again for 5 min before incubation with PI(4,5)P_2, as previously described (Hughes et al., 2018b), and then frozen on grids. Condition 2 revealed one structure without a PI(4,5)P_2 density, TRPV5pH6-state3, at 2.6 Å resolution (Figures 2D, 2I, and S5; Table 1).

While all three structures were resolved at similar resolutions, the PI(4,5)P_2 density was observed only in the TRPV5$_{pH6+PIP2-state1}$ structure (Figures 3G, 3K, and 3O), where the protein was at pH 6.0 for only a short period of time before freezing. The structure of TRPV5$_{pH6+PIP2-state1}$ resembled our previously determined TRPV5 PI(4,5)P_2 bound structure at pH 8.0, referred to as TRPV5$_{pH8+PIP2}$ (PDB: 6DMU) (Hughes et al., 2018b) (Figures 2A, 2F, 3A, 3F, 3J, and 3N). TRPV5$_{pH6+PIP2-state1}$ had PI(4,5)P_2 fully engaging with the channel (Figure 3G); the pore radius at Ile575 in the TRPV5$_{pH6+PIP2-state1}$ structure was around 2.7 Å, while in TRPV5$_{pH8+PIP2}$ it was around 3.3 Å (Figure S3A). Interestingly, the Asp542 in TRPV5$_{pH6+PIP2-state1}$ was facing the pore vestibule, which differs from the previously observed conformation of Asp542 in TRPV5$_{pH8+PIP2}$ (Figures 2A, 2B, 2E, and S3A). Asp542 has been shown to adopt two conformations, which is consistent with its dynamic nature, and the upward conformation has been noted only upon PI(4,5)P_2 binding at pH 8.0 (Hughes et al., 2018b). Moreover, the salt-bridge networks in the TRPV5$_{pH6+PIP2-state1}$ between Lys607 and Asp406 and between Arg409 and Glu294 were starting to form (Figures 2G, S4C, and S4D).

The TRPV5$_{pH6-state2}$ structure did not have bound PI(4,5)P_2, the pore radius at Ile575 was around 1.1 Å, and all salt bridges at Arg606, Lys607, and Asp406 and at Arg409 and Glu294 were almost fully formed, as similarly observed in TRPV5$_{pH6}$ (Figures 2C, 2E, 2H, S4C, and S4D). To understand how low pH inhibits TRPV5 after PI(4,5)P_2 activation, we again aligned to the tetrameric pore and made comparisons between the TRPV5$_{pH8+PIP2}$, the TRPV5$_{pH6+PIP2-state1}$, and the TRPV5$_{pH6-state2}$ structures. The formation of salt bridges near the proposed intracellular pH sensor Lys607 leads to significant conformational changes in TRPV5$_{pH6+PIP2-state1}$ compared with TRPV5$_{pH8+PIP2}$. In TRPV5$_{pH6+PIP2-state1}$, the ARD shifted upward 4.8 Å and rotated by 3.5°, which was also accompanied by overall movements of 2.2 Å in the S1–S4 bundle, 1.6 Å in the S4–S5 linker, and 1.1 Å in S5 and a 2.0 Å upward movement at the beginning of the TRP helix (Figures 4A and 4B). Also, in TRPV5$_{pH6+PIP2-state1}$, the S6 helix moved 0.9 Å to constrict the pore but was otherwise in a position similar to that in TRPV5$_{pH8+PIP2}$. The conformational changes seen in the TRPV5$_{pH6+PIP2-state1}$ structure seemed to be on the transition to the TRPV5$_{pH6-state2}$

structure, which had the same, yet larger, movements compared with $TRPV5_{pH8+PIP2}$. In $TRPV5_{pH6\text{-}state2}$ the ARD shifted upward 4.8 Å and rotated by 6.5°, which was also accompanied by an overall movement of 2.4 Å in the S1–S4 bundle, 2.2 Å in the S4–S5 linker, and 1.7 Å in S5 and a 5.0 Å upward movement at the beginning of TRP helix. Also, in $TRPV5_{pH6\text{-}state2}$, the S6 helix moved by 2.3 Å to constrict the pore in a position similar to that in $TRPV5_{pH6}$, but with Trp583 in a position similar to that in $TRPV5_{pH8}$ (Figures 1C, 2C, 4A, and S3A).

While the structures of the channel found in condition 1 indicated that low pH induced conformational changes involved in closing the channel, our condition 2, where $PI(4,5)P_2$ was added to the channel protein already at pH 6.0, probed how low pH affects $PI(4,5)P_2$ interaction with the channel. First, we compared $TRPV5_{pH6\text{-}state3}$ and $TRPV5_{pH6}$ (Figures 4C and 4D) and noticed that these structures are very similar (Figures 4C and 4D). Yet, the notable difference between $TRPV5_{pH6\text{-}state3}$ and $TRPV5_{pH6}$ is the position of Ile575, which allowed the $TRPV5_{pH6\text{-}state3}$ pore to adopt a wider radius of 2.1 Å compared with the $TRPV5_{pH6}$ structure at 1.2 Å, confirmed by the model fit to the density (Figures 1B, 1C, 2D, 2E, and S3A). Both the $TRPV5_{pH6\text{-}state3}$ and the $TRPV5_{pH6}$ structures had similar conformational changes compared with the $TRPV5_{pH8+PIP2}$ structure, including a 6.2 Å upward shift and 5° rotation of the ARD, as well as overall movements of 2.3 Å in the S1–S4 bundle, 1.9 Å in the S4–S5 linker, 1.5 Å in S5, and 1.7 Å in S6 and a 4.6 Å upward movement at the start of the TRP helix (Figures 4C and 4D). In addition, $PI(4,5)P_2$ was not resolved bound to the $TRPV5_{pH6\text{-}state3}$ channel (Figure 3H), and all key positively charged coordinating residues (Arg302, Arg305, Lys484, and Arg584) were not engaged at this site, suggesting that low pH prevents $PI(4,5)P_2$ from binding (Figures 3H and 3L). This was also confirmed by calculating the electrostatic potential in the $PI(4,5)P_2$ binding site, which revealed less positive charge and reduced binding pocket surface area in $TRPV5_{pH6\text{-}state3}$ compared with $TRPV5_{pH6+PIP2\text{-}state1}$ and $TRPV5_{pH8+PIP2}$ (Figures 3N–3P). However, under condition 2, we captured TRPV5 in an intermediate, partially open, conformation, suggesting possible transient interactions with $PI(4,5)P_2$ (Figures 3C, 3E, and 3H). We would like to note that under both conditions, lowering the pH again did not have an effect on the extracellular pH sensor Glu522 (Figure 2J).

To test the functional importance of the salt-bridge formation between the Lys607 and the Asp406 residues, we mutated the Asp406 residue to Ala (Asp406Ala). We found that this mutation had a profound effect on inhibition by intracellular low pH. Figures 4E and 4F show excised inside-out patch-clamp measurements after current rundown and reactivation by diC_8 $PI(4,5)P_2$. Changing the pH of the perfusion solution from pH 7.4 to pH 6.4 inhibited wild-type TRPV5 channel activity by 58.5 ± 6.4%. The D406A mutant, on the other hand, was not inhibited by pH 6.4, but rather its activity increased by 64.4 ± 11.3%.

TRPV5 modulation by PKA

To investigate the effects of post-translational modification by PKA on TRPV5 (de Groot et al., 2009, 2011), we first performed a phosphorylation assay to confirm that the purified TRPV5 protein in detergent could be phosphorylated by the catalytic subunit of PKA (PKA_{cat}) (Figure S6A). Mass spectrometry confirmed that the Thr709 residue in TRPV5 is

phosphorylated under these *in vitro* conditions (see STAR Methods). Next, we utilized cryo-EM under the same experimental conditions to solve the structure of TRPV5 in the presence of PKA_{cat} ($TRPV5_{PKA}$) at pH 8.0 (Figures S6B–S6F). Extensive computational sorting was employed in cryoSPARC (see STAR Methods, Table 1) and we consistently noted that only one class contained an extra density in the ARD "skirt" in this dataset (Figure S6G). Similar observations were made by our group when we solved the TRPV5 CaM-bound structure (Figure S6H). Thus, knowing that CaM and PKA_{cat} both interact with the distal C terminus of the channel and involve Thr709 for its binding, we attributed this density to the PKA_{cat} (Figure S6G). The $TRPV5_{PKA}$ structure was resolved in C1 symmetry and reached only 4.5 Å resolution, which did not allow us to determine atomic details between PKA_{cat} and the channel (Figures S6B–S6F). Efforts to resolve the TRPV5 structure in the presence of PKA_{cat} to higher resolution and in better detail using all currently available methods were not successful (see STAR Methods). Therefore, we compared this structure with only the CaM-bound TRPV5 by low-pass filtering to 10 Å resolution (Figure S6H). This comparison allowed us to conclude that PKA_{cat} likely interacts with the distal C terminus of the channel transiently, while CaM tightly binds the C terminus and pore of the channel, allowing the TRPV5-CaM structure to be resolved to higher resolution (Figures S6G and S6H). This is not surprising, since the function of a kinase is to phosphorylate its target, for which a stable interaction may not be necessary.

Next, due to the transient nature of the complex, we investigated the effect of PKA phosphorylation specifically at the Thr709 residue. We made the Thr709Asp phosphomimetic TRPV5 mutant to simulate PKA phosphorylation at this site, as it has been implemented in previous functional studies (de Groot et al., 2009, 2011). In a cellular environment, TRPV5 is exposed to both $PI(4,5)P_2$ and PKA concurrently. To test our hypothesis on the interplay between $PI(4,5)P_2$ and phosphorylation on TRPV5 gating, we used cryo-EM to solve TRPV5 Thr709Asp mutant ($TRPV5_{T709D}$) structures with and without $PI(4,5)P_2$. Structures of $TRPV5_{T709D}$ and $TRPV5_{T709D+PIP2}$ were solved to 2.8 and 3.4 Å resolution, respectively (Figure S7, Table 1). The state of $TRPV5_{T709D}$ largely resembles $TRPV5_{pH8}$ at the pore region (Figures 5A and 5B), with minimal conformational changes at the ARDs region of the channel (all-atom root-mean-square deviation [RMSD] 1.08 for $TRPV5_{T709D}$ versus $TRPV5_{pH8}$) (Figures 5E–5G). On the other hand, the $TRPV5_{T709D+PIP2}$ structure was captured at a new intermediate conformation, different from the original fully open $TRPV5_{pH8+PIP2}$ structure (Figure 3). Interestingly, it also differs from the newly obtained partially open intermediates $TRPV5_{pH6+PIP2\text{-}state1}$ and $TRPV5_{pH6\text{-}state3}$ (Figure 3).

In the $TRPV5_{T709D+PIP2}$ structure, $PI(4,5)P_2$ was resolved at the same binding site as in the $TRPV5_{pH8+PIP2}$ structure and located between the N linker, the S2–S3 linker, the S4–S5 linker, and the S6 helix (Figure 3). Binding in this pocket induced the conformational changes needed to open the lower gate, yet the pore radius measured at Ile575 in the $TRPV5_{T709D+PIP2}$ structure is around 2.4 Å, compared with the fully open $TRPV5_{pH8+PIP2}$ structure (around 3.3 Å) (Figures 5E and S3B). In addition, Asp542 was resolved facing the pore vestibule due to the dynamic nature of the selectivity filter, differing from the $TRPV5_{pH8+PIP2}$ state (Figures 5 and S3). Moreover, the channel underwent several conformational changes that differ from the fully open $TRPV5_{pH8+PIP2}$ (Figures 5H and 5I).

In $TRPV5_{T709D+PIP2}$ structure, the ARD shifts upward 5 Å and rotates by 3.5° compared with $TRPV5_{pH8+PIP2}$, which is also accompanied by an overall movement of 2.0 Å in the S1–S4 bundle, 1.5 Å in the S4–S5 linker, and 1.0 Å in S5 and a 2.3 Å upward movement at the beginning of the TRP helix (Figures 5H and 5I). Interestingly, when we compared $TRPV5_{pH8+PIP2}$ and $TRPV5_{T709D+PIP2}$ structures, it became evident that the Thr709Asp phosphomimetic mutation is influencing the position of the ARDs in the TRPV5 structure, but not the opening of the channel (Figures 5H and 5I). It seemed that $PI(4,5)P_2$, as the endogenous modulator, was predominantly responsible for stabilizing the open state of the TRPV5. To further test this hypothesis, we measured wild-type and Thr709Asp TRPV5 activity in excised inside-out patch-clamp recordings. A rundown of currents following membrane excision was observed in both wild type and TRPV5 Thr709Asp mutant. This rundown is typical of $PI(4,5)P_2$-dependent ion channels and is caused by dephosphorylation of $PI(4,5)P_2$ by lipid phosphatases in the patch membrane. Application of diC_8 $PI(4,5)P_2$ in the perfusion restored channel activity for both Thr709Asp mutant and wildtype TRPV5. Since current amplitudes in excised patch recordings are highly variable between oocytes, we normalized current amplitudes to those at 50 μM diC_8 $PI(4,5)P_2$. As shown in Figures 5J and 5K, the Thr709Asp mutation did not alter TRPV5 dependence on diC_8 $PI(4,5)P_2$, and different concentrations of diC_8 $PI(4,5)P_2$ evoked currents at comparable magnitudes.

As indicated by previous studies, the binding of CaM to the TRPV5 Thr709Asp mutant is partially impaired, as seen through pull-down assays (de Groot et al., 2011). To further investigate the effects of Thr709 phosphorylation on channel gating, the interaction between TRPV5 Thr709Asp mutant and CaM was further examined through cryo-EM structural studies. Structural studies were performed on the nanodisc-reconstituted TRPV5 Thr709Asp mutant incubated with CaM in the presence of calcium ($TRPV5_{T709D+CaM}$). Data processing revealed the $TRPV5_{T709D+CaM}$ structure at 3.0 Å resolution and no density that could be attributed to CaM. The $TRPV5_{T709D+CaM}$ structure was identical to the $TRPV5_{pH8}$ and $TRPV5_{T709D}$ structures (Figures S6I, S6J, and S7; Table 1).

DISCUSSION

TRPV5 is a highly selective calcium channel that is primarily expressed in the kidney and plays an essential role in calcium reabsorption (Peng, 2011; van der Wijst et al., 2019; van Goor et al., 2017). TRPV5 gating is tightly regulated by numerous endogenous modulators to precisely control calcium influx (de Groot et al., 2011; Lee et al., 2005; Peng, 2011; van der Wijst et al., 2019). In this study, we have presented molecular details of the interplay between $PI(4,5)P_2$, pH, CaM, and PKA phosphorylation on TRPV5 gating.

$PI(4,5)P_2$ is a general regulator of many different ion channels, including TRP channels. For the majority of ion channels, $PI(4,5)P_2$ acts as an obligate co-factor necessary for channel activity (Suh and Hille, 2008). Phosphoinositide regulation of TRP channels is more complex in many cases, but for the vast majority of TRP channels, $PI(4,5)P_2$ acts as a positive regulator (Rohacs, 2014). Most TRP channels require additional factors to open, but TRPV5 and its close relative TRPV6 are opened by resting levels of $PI(4,5)P_2$ alone (Rohacs, 2014), making them constitutively active. Thus, these channels are ideal model systems to understand the molecular mechanism of channel opening by this core

regulator. Currently, the only published TRP channel structure where $PI(4,5)P_2$ is resolved, and induces an open conformation, is our previously published TRPV5 structure at 4 Å resolution (Hughes et al., 2018b). Here, we determined two new structures of TRPV5 with $PI(4,5)P_2$, at 2.8 Å for $TRPV5_{pH6+PIP2\text{-}state1}$ and at 3.4 Å for $TRPV5_{T709D+PIP2}$. In both cases, we clearly resolved the $PI(4,5)P_2$ density in the previously proposed $PI(4,5)P_2$ binding site (Hughes et al., 2018b) and showed that addition of $PI(4,5)P_2$ to the channel clearly produced conformational changes, which substantially increased TRPV5 pore diameter compared with the structure without $PI(4,5)P_2$. These results provide a solid structural basis for channel opening by the key endogenous gating molecule $PI(4,5)P_2$.

Metabolic acidosis is a pathophysiological condition characterized by acid-base imbalance in the body, and it is common in people with kidney disease (Wagner and Mohebbi, 2010). It has been shown that TRPV5-dependent Ca^{2+} reabsorption decreases during chronic metabolic acidosis and leads to kidney stone formation, suggesting that extracellular protons inhibit the channel (Na and Peng, 2014; Wagner and Mohebbi, 2010). Moreover, it has been shown that not only extracellular pH, but also intracellular protons regulate TRPV5 and have similar effects on single-channel properties of the channel (Yeh et al., 2003, 2005). In this study, we established that lowering of pH leads to the channel closing through the formation of the salt bridges around the proposed intracellular pH sensor Lys607 in the channel (Cha et al., 2007) and the hindrance of $PI(4,5)P_2$ interaction with TRPV5. The role of the salt bridge between Lys607 and Asp406 is supported both by our finding that the Asp406Ala mutation eliminated inhibition of TRPV5 by pH 6.4 in excised inside-out patches and by earlier findings that neutralization of the Lys607 residue reduced inhibition by low intracellular pH (Yeh et al., 2005). In addition, Asp406 was previously implicated in the binding site of the TRPV5 inhibitor ZINC17988990, highlighting its role in channel inhibition (Hughes et al., 2019). In addition, we showed that lowering the pH did not have an effect on the position of the extracellular pH sensor Glu522 in the structures (Yeh et al., 2003, 2006); nevertheless, it could be that cross talk between intracellular and extracellular TRPV5 sensors has an additive effect on channel opening and closing (Cha et al., 2007).

We determined three structures of TRPV5 with added $PI(4,5)P_2$ at pH 6.0. The lipid density was detectable only in a subpopulation of the images where the channel was preincubated at pH 8.0 with $PI(4,5)P_2$ and pH was lowered to 6.0 only before freezing the samples ($TRPV5_{pH6+PIP2\text{-}state1}$). This suggests that we captured the channel in the process of $PI(4,5)P_2$ dissociating from the protein. When the channel protein was kept at pH 6.0 before the addition of $PI(4,5)P_2$ the lipid density was absent ($TRPV5_{pH6\text{-}state3}$), indicating that low pH prevented lipid binding to the protein. Intriguingly, our results are in agreement with a recently proposed computational model for TRPV5 modulation by $PI(4,5)P_2$ (Fathizadeh et al., 2021), which suggested that binding of $PI(4,5)P_2$ to the channel depends on the protonation state of the lipid. Establishing whether $PI(4,5)P_2$ dissociation from the channel is primarily caused by protonation of the lipid, conformational changes in the protein, or their combination will require more work. Overall, our data indicate that both conformational changes around the S2–S3 and the TRP helix that prevent the channel from opening, together with the disruption of the $PI(4,5)P_2$-protein interaction, lead to channel closing.

Our results on TRPV5 gating by PKA revealed that PKA transiently interacts with the channel at the distal C terminus and has minimal effect on overall conformational changes. Yet, it supports a previously proposed model, which suggested that TRPV5 phosphorylation by PKA at Thr709 abolishes CaM binding to TRPV5 (de Groot et al., 2009, 2011), causing TRPV5 to remain in the open/activated state but only in the presence of $PI(4,5)P_2$. Our structures of $TRPV5_{T709D}$ and $TRPV5_{T709D+PIP2}$ showed states similar to $TRPV5_{pH8}$ and $TRPV5_{pH8+PIP2}$, respectively. One noticeable difference was observed between the $TRPV5_{pH8+PIP2}$ and the $TRPV5_{T709D+PIP2}$ structures: the $TRPV5_{T709D+PIP2}$ pore did not capture a fully open state. This is perhaps because we could resolve only a transitional state of the channel on the way to a fully open state or the Thr709Asp phosphomimic mutation affects the maximum pore opening. Our results again confirmed that $PI(4,5)P_2$ is an indispensable activator of TRPV5 (Hughes et al., 2018b; Lee et al., 2005; Rohacs et al., 2005) and showed that PKA phosphorylation alone does not open the channel (de Groot et al., 2009, 2011), but likely increases channel activity by preventing inhibition by CaM.

TRPV5 and TRPV6 are closely related epithelial Ca^{2+} channels, the products of a relatively recent gene duplication (Na and Peng, 2014; Peng, 2011). These two channels share 80% sequence homology (Figure S2) and they have very high functional similarity with each other, more than with other members of the TRPV subfamily (Na and Peng, 2014; Peng, 2011). While there is no TRPV6 channel structure in the presence of $PI(4,5)\ P_2$ available, computational modeling and mutational analysis indicate that $PI(4,5)P_2$ binds to TRPV6 at the same conserved site as to TRPV5 (Hughes et al., 2018b) (Figure S2). The co-structure of TRPV6 with CaM (Singh et al., 2018) is very similar to the two available TRPV5-CaM co-structures (Dang et al., 2019; Hughes et al., 2018b), showing binding of CaM to equivalent residues and pore block by the same residue in CaM as in TRPV5. TRPV6 is also inhibited by low pH (Peng et al., 1999), and the equivalent residue that is phosphorylated by PKA in the distal C-terminal CaM binding site in TRPV5 was shown to be phosphorylated by protein kinase C (PKC) in human TRPV6, relieving CaM inhibition (Niemeyer et al., 2001). These structural and functional similarities between TRPV5 and TRPV6 indicate that some, or all, of our data may also be relevant for understanding the mechanism of gating of TRPV6.

Overall, these studies gave new structural and molecular insights into TRPV5 gating by $PI(4,5)P_2$, pH, CaM, and PKA. Based on our data, we propose that low pH acts as a modulator of TRPV5 gating though formation of salt bridges around Lys607 and alteration of $PI(4,5)P_2$ binding to the channel, which subsequently leads to channel closing (Figure 6A). In addition, we propose that phosphorylation of TRPV5 by PKA does not directly activate the channel, in agreement with the previously proposed model (de Groot et al., 2011), and that phosphorylated TRPV5 still requires $PI(4,5)P_2$ to open (Figure 6B). Nevertheless, PKA phosphorylation of TRPV5 at residue Thr709 prevents CaM binding and channel inactivation, allowing more calcium to enter the cell. Our results provide detailed insight into the mechanisms of TRPV5 modulation by endogenous modulators at the molecular level, potentially aiding in the development of novel therapeutics to treat hypercalciuria, nephrolithiasis, and osteoporosis.

Limitations of the study

In this study we determined the mechanism of TRPV5 modulation by lower pH. In structural studies, the pH of the whole sample is altered; thus, specific effects of the extracellular and intracellular pH cannot be evaluated, unlike in electrophysiology experiments. In addition, we were able to investigate only the effect of pH 6.0 on the TRPV5 channel, as lowering pH further, such as to pH 5.0, severely affected sample quality. Another limitation of the study is that, while we attempted to resolve the complex between $TRPV5_{T709D}$ and CaM, we were unable to resolve any density attributed to CaM. While this is compatible with the notion that phosphorylation reduced or eliminated binding of CaM to the channel, we are unable to make firm conclusions on the apparent affinity or the binding state of the phosphomimetic mutant of TRPV5 to CaM.

STAR★METHODS

RESOURCE AVAILABILITY

Lead contact—Further information and requests for either resources or reagents should be directed to and will be fulfilled by the lead contact, Vera Moiseenkova-Bell (vmb@pennmedicine.upenn.edu).

Materials availability—Requests for materials generated in this study should be directed to and will be fulfilled by the lead contact Vera Moiseenkova-Bell (vmb@pennmedicine.upenn.edu).

Data and code availability—All data generated in these studies are available upon request from lead contact Vera Moiseenkova-Bell (vmb@pennmedicine.upenn. edu). The cryo-EM density maps and atomic coordinates have been deposited into the Electron Microscopy Data Bank (EMDB) and Protein Data Bank (PDB), respectively. Accession codes are as follows: $TRPV5_{pH8}$ (EMDB: 25716, PDB: 7T6J); $TRPV5_{pH6}$ (EMDB: 25717, PDB: 7T6K); $TRPV5_{pH5}$ (EMDB: 25718, PDB: 7T6L); $TRPV5_{pH6+PIP2\text{-}state1}$ (EMDB: 25719, PDB: 7T6M); $TRPV5_{pH6\text{-}state2}$ (EMDB: 25720, PDB: 7T6N); $TRPV5_{pH6\text{-}state3}$ (EMDB: 25721, PDB: 7T6O); $TRPV5_{PKA}$ (EMDB: 25722); $TRPV5_{T709D}$ (EMDB: 25723, PDB: 7T6P); $TRPV5_{T709D+PIP2}$ (EMDB: 25724, PDB: 7T6Q); and $TRPV5_{T709D+CaM}$ (EMDB: 25725, PDB: 7T6R). Accession numbers are listed in the key resources table. This paper does not report original code. Any additional information required to reanalyze the data reported in this paper is available from the lead contact upon request.

EXPERIMENTAL MODEL AND SUBJECT DETAILS

For expression of TRPV5 channel in structural studies, BJ5457 Saccharomyces cerevisiae (ATCC) was transfected with a YepM plasmid bearing rabbit TRPV5 sequence with 1D4 epitope tag and maintained at 30°C. For expression of rat calmodulin, BL21(DE3) competent *Escherichia coli* were transformed with a pET28b plasmid bearing the rat calmodulin sequence for inducible expression at 37°C. For expression of TRPV5 channel in electrophysiological studies, oocytes from Xenopus Laevis were microinjected with cRNA encoding for rabbit TRPV5 and maintained at 18°C. Additional details can be found in the method details.

METHOD DETAILS

Xenopus oocyte preparation and injection—Xenopus Laevis frogs (Xenopus Express) were anesthetized in Tricaine-S solution (0.5 g/L) and oocytes were extracted by the following sterile surgery protocol: Following a small (~1 cm) incision on the abdomen, the skin and the muscle were cut with scissors. Oocyte sacks were collected gently with forceps and the incision was closed with suture (Oasis PGA Absorbable Suture). The collected oocytes were digested in 0.2 mg/mL collagenase (Sigma) in OR2 solution (82.5 mM NaCl, 2 mM KCl, 1 mM $MgCl_2$, and 5 mM HEPES, pH 7.4) rotating overnight at 18°C. The defolliculated oocytes were washed three times in OR2 and placed in OR2+ solution (OR2 solution supplemented with 1% penicillin/streptomycin and 1.8 mM $CaCl_2$) and kept at 18°C. Healthy oocytes were hand-selected under a microscope and were microinjected with cRNA using a nanoliter injector system (World Precision Instruments). cRNA for this procedure was prepared by mMessage mMachine T7 kit (Thermo Fisher) using wildtype or mutated rabbit TRPV5 DNA as template. Point mutations were generated by Quikchange XL mutagenesis kit (Agilent Genomics).

Electrophysiology—Two electrode voltage clamp experiments were performed as described earlier (Velisetty et al., 2016). Briefly, oocytes were bathed in a solution containing 97 mM NaCl, 2 mM KCl, 1 mM $MgCl_2$, 5 mM HEPES, pH 7.4. TRPV5 currents are blocked by Mg^{2+} and trace amounts of Ca^{2+} present in this solution. Monovalent currents were initiated by removing Mg^{2+} and traces of Ca^{2+} by switching to a solution containing 96 mM LiCl, 1 mM EGTA, and 5 mM HEPES, pH 7.4. LiCl is used as a charge carrier for monovalent currents, as it minimizes endogenous currents in non-injected oocytes in divalent free solutions. Both microelectrodes were placed in thin-wall inner filament-containing glass pipettes (World Precision Instruments) filled with 3 M KCl in 1% agarose. Currents were collected with a GeneClamp 500B amplifier (Molecular Devices). A ramp protocol from −100 to +100 mV (0.25 mV/ms) with a holding potential at 0 mV was applied. The pCLAMP software (Molecular Devices) was used for data collection and analysis.

Excised inside-out patch clamp experiments were performed as described earlier (Velisetty et al., 2016). Patch clamp glass (World Precision Instruments PG10152–4) were pulled (Sutter Instruments) to get pipettes with 0.6–1.3 MΩ resistance. Pipettes were filled with the solution containing 96 mM LiCl, 1 mM EGTA, and 5 mM HEPES, pH 7.4. The oocytes were placed in bath solution containing 96 mM KCl, 5 mM EGTA, and 10 mM HEPES, pH 7.4 and devitellinized carefully by using sharp forceps. Following formation of the gigaohm seal, a ramp protocol from − 100 to +100 mV (0.25 mV/ms), immediately preceded by a 100-ms step to −100 mV was performed. diC_8 $PI(4,5)P_2$ (Cayman) was dissolved in bath solution and applied to the intracellular side of the patch membrane through a custom made perfusion system.

Cloning—The YepM TRPV5 Thr709Asp mutant vector for protein expression in S. cerevisiae was produced using a ligation-free cloning approach to introduce the point mutation with primers. (See key resources table). YepM TRPV5 WT was used as a template and run through 18 cycles of PCR with primers and Phusion master mix. Product

was digested using DpnI restriction enzyme to remove the template and the result was transformed and purified in XL-Gold bacterial cells. Plasmid was sequenced to confirm incorporation of the mutation.

TRPV5 protein preparation—TRPV5 was prepared as previously described (Hughes et al., 2018b) and outlined (Fluck et al., 2021). TRPV5 with a C-terminal 1D4 epitope tag was expressed in S. cerevisiae using a YepM vector (Moiseenkova-Bell et al., 2008) transfected into BJ5457 *Saccharomyces cerevisiae* (ATCC) using an alkali-cation yeast transformation kit (MP Biomedicals) according to the manufacturer's instruction. Cells were plated onto SD-Leu agar plates and allowed to grow at 30°C for 2 days. Half of the colonies were picked from one plate and inoculated into a single 75 mL starter culture containing SD-Leu media and 10% *v*/v glycerol. The starter culture was allowed to grow at 30°C until the OD reached the top of the log phase (OD 1.0–1.4). About 2 mL of this culture was inoculated into another 125 mL starter culture, and the cells were checked for TRPV5 expression by Western blot with the 1D4 antibody (Hodges et al., 1988). Once expression was confirmed, the cells were grown at 30°C shaking at 200 RPM in 2.5 L of media per flask until the OD reached the top of the log phase (OD 1.0–1.4). Cells were harvested by centrifugation at 3000 × *g*, resuspended in storage buffer (25 mM Tris-HCl, pH 8.0, 300 mM Sucrose, and 1 mM PMSF) on ice, then spun down at 3000 × *g*, discarding the supernatant. Cell pellets were then stored at −80°C. This expression culture was propagated with 15 mL of the previous growth at OD 1.0–1.4 for multiple days until the desired amount was grown. All subsequent steps were carried out at 4°C unless noted otherwise. Cells from approximately 60 L of growth were thawed and resuspended in 300 mL of homogenization buffer (25 mM Tris-HCl, pH 8.0, 300 mM Sucrose, 5 mM EDTA, and protease inhibitor cocktail). Resuspended cells were lysed using a M110Y microfluidizer (Microfluidics) at 100 psi. The membranes were separated from cellular debris via centrifugation at 3,000 × *g* for 10 min and subsequent centrifugation of the supernatant at 14,000 × *g* for 35 min. Then using the previous spin's supernatant, the membranes were pelleted at 100,000 × *g* for 1 h. Pelleted membranes were harvested and resuspended on ice using a 15 mL tissue homogenizer (Kontes Duall with PTFE pestle) in buffer containing 25 mM Tris-HCl, pH 8.0, 300 mM Sucrose, and 1 mM PMSF then stored at −80°C. TRPV5 was solubilized from the thawed membranes in solubilization buffer (20 mM HEPES, pH 8.0, 150 mM NaCl, 2 mM TCEP, and 0.87 mM LMNG). The insoluble fraction was separated by centrifugation at 100,000 × *g* for 1 h. The supernatant was incubated with 1D4-antibody coupled to CnBr-activated Sepharose beads for 3 h. The beads were collected on a gravity flow column and washed with wash buffer containing 20 mM HEPES, pH 8.0, 150 mM NaCl, 2 mM TCEP, and 0.064 mM DMNG. The beads were incubated with elution buffer (20 mM HEPES, pH 8.0, 150 mM NaCl, 2 mM TCEP, and 0.064 mM DMNG, 3 mg/mL 1D4 peptide) overnight. TRPV5 was eluted once every 5 min in ten 1 mL fractions. Peak fractions were pooled and concentrated using a 100-kDa concentrator (Millipore). To reconstitute TRPV5 into nanodiscs, an equimolar quantity of MSP2N2 protein (Grinkova et al., 2010) was incubated with the detergent-solubilized TRPV5 in the presence of soy polar lipids and DMNG detergent in a reaction volume of 1 mL. The ratio in the mixture of TRPV5:MSP2N2:Lipid:DMNG was 1:1:200:500. The reaction mixture was incubated on ice for 30 min, then about 30 μL of Bio-Beads were added before rotating at 4°C for

1 h. The mixture was pipetted off of the used Bio-Beads into a new tube, then 30 μL of fresh Bio-Beads were added before rotating at 4°C overnight to complete the reaction. The reconstituted TRPV5 was run on a Superose 6 increase 10/300 GL column (GE Healthcare) equilibrated with 20 mM HEPES, pH 8.0, 150 mM NaCl, 2 mM TCEP. Fractions containing nanodisc-reconstituted TRPV5 were pooled and concentrated.

PKA phosphorylation assay and mass spectrometry—1 unit of PKA_{cat} (New England Biolabs) was reacted with 1 ng of TRPV5 at 4°C. Activity was measured using the Biovision Universal Kinase Assay kit according to manufacturer's instruction. The fluorescence Ex/Em = 535/587 nm was read on a plate reader and signal was measured over time. To confirm the residue being phosphorylated, 6.15 μM TRPV5 was incubated with 250 μM ATP, 12.5 mM $MgCl_2$ and 1 unit of PKA for 16 h. Mass spectrometry was performed on the TRPV5 band from SDS-PAGE of this sample to confirm phosphorylation of residue Thr709.

CaM expression and purification—Rat CaM in a pET28b vector was expressed in BL21(DE3) *Escherichia coli*. Cells were transformed then grown at 37°C in Terrific Broth (TB) supplemented with 30 μg/mL kanamycin. Expression was induced at OD 0.7 with 1 mM ITPG and grown for 4 h. Cells were harvested by centrifugation at 3000 × *g* and stored at −80°C. Cells were thawed and resuspended in buffer containing 50 mM Tris-HCl, pH 7.5, 2 mM EDTA, and a complete EDTA-free protease inhibitor cocktail tablet (Roche). The cells were broken in a M110Y microfluidizer at 80 psi and the lysate was spun at 20000 × *g* for 1 h to remove cellular debris. The supernatant was collected and supplemented with 5 mM $CaCl_2$. At room temperature, a HiTrap phenyl sepharose low sub fast flow column (Cytiva) was equilibrated in 10 CV of equilibration buffer (50 mM Tris-HCl, pH 7.5, 5 mM $CaCl_2$, 100 mM NaCl). Lysate was applied to the column and 10 CV of wash buffer (50 mM Tris-HCl, pH 7.5, 0.1 mM $CaCl_2$, 100 mM NaCl) was used. A high salt wash (50 mM Tris-HCl, pH 7.5, 0.1 mM $CaCl_2$, 500 mM NaCl) was applied, then the protein was eluted using elution buffer (50 mM Tris-HCl, pH 7.5, 1 mM EGTA) into 1 mL fractions. Fractions containing protein were pooled and concentrated to 1 mL using a 10-kDa concentrator (Millipore). Protein was further purified using size exclusion chromatography on a Superdex S75 16/600 column (GE Healthcare) equilibrated with buffer containing 10 mM Tris-HCl, pH 7.5, 10 mM $CaCl_2$, 50 mM NaCl.

Cryo-EM sample preparation and data collection—All TRPV5 samples were processed similarly (Table 1). Samples $TRPV5_{pH6}$, $TRPV5_{pH5}$ with lower pH were spiked with sodium acetate pH 5.0 to adjust to desired pH 5 min before freezing. Sample $TRPV5_{PIP2+pH6}$ was incubated for 45 min with 400 μM diC8-$PI(4,5)P_2$ (Echelon Biosciences) then spiked with sodium acetate pH 5.0 to adjust to pH 6.0 before sample freezing. Sample $TRPV5_{pH6\text{-}state3}$ was first spiked with sodium acetate pH 5.0 to adjust to pH 6.0 then incubated with 400 μM diC8-$PI(4,5)P_2$ for 45 min before sample freezing. Sample $TRPV5_{PKA}$ was made by incubating TRPV5 (0.96 mg) with PKA_{cat} (2.6 U) in the presence of 420 μM ATP and 21 mM $MgCl_2$ for 16 h in a total volume of 310 μL before sample freezing. Samples $TRPV5_{pH8}$ and $TRPV5_{T709D}$ were frozen directly after protein purification. $TRPV5_{T709D+CaM}$ was purified by first combining purified $TRPV5_{T709D}$ in

nanodiscs with purified rat CaM in a 1:20 molar ratio supplemented with 10 mM $CaCl_2$ for 1 h. This mixture was then purified on a Superose 6 increase 10/300 GL column (GE Healthcare) equilibrated with 20 mM HEPES, pH 8.0, 150 mM NaCl, 2 mM TCEP. $TRPV5_{T709D+CaM}$ was concentrated and then frozen. Using a Vitrobot Mark IV (Thermo Scientific), 3 μL of the samples were applied onto glow-discharged 1.2/1.3 Quantifoil Holey Carbon Grids (Quantifoil Micro Tools). The sample was blotted in a chamber at 4°C and 100% humidity for 6–9 s with 0 blot force before being frozen in liquid ethane. $TRPV5_{PKA}$ sample was imaged on a Titan Krios 300 kV electron microscope with a Gatan K2 direct electron detector. 60 frame movies were collected with a nominal dose of 72 $e^{-}/Å^2$. Super-resolution images for the $TRPV5_{PKA}$ dataset were collected at a magnification of 130,000 and had a pixel size of 0.535 Å/pixel. All other samples were imaged on a Titan Krios G3i 300 kV electron microscope with a Gatan K3 direct electron detector. 40 frame movies were collected with a nominal dose of 42 $e^{-}/Å^2$. Super-resolution images for $TRPV5_{pH8}$, $TRPV5_{pH5}$, $TRPV5_{pH6\text{-}state3}$, and $TRPV5_{T709D+CaM}$ datasets were collected at a magnification of 105,000 and had a pixel size of 0.415 Å/pixel. Super-resolution images for $TRPV5_{pH6}$, $TRPV5_{PIP2+pH6}$, $TRPV5_{T709D}$, and $TRPV5_{T709D+PIP2}$ datasets were collected at a magnification of 81,000 and had a pixel size of 0.53 Å/pixel.

Data processing—All datasets were processed similarly using cryoSPARC v3.2.0 (Punjani and Fleet, 2021; Punjani et al., 2017, 2020). For the $TRPV5_{pH8}$ dataset, 2,350 movies were collected. Movies were patch motion corrected with an alignment resolution of 3 Å and Fourier cropped to half the resolution. The micrographs were then run through patch CTF estimation. The micrographs were then autopicked using 2D templates generated from a subset of 100 micrographs. 242,844 particles were extracted and binned by a factor of 2 with a box size of 144 pixels and sorted with 2D classification. 111,116 particles remained after 1 round of 2D classification. Ab-initio reconstruction with 1 class was used to generate the initial structure. These particles were then subjected to heterogeneous refinement with 5 classes. One class with 54,415 particles was taken and particles were extracted in an unbinned box size of 288 pixels. Particles were subjected to Non-uniform (NU) refinement in C1 symmetry (3.5 Å) and subsequently C4 symmetry (3.2 Å). Global and local CTF refinement were performed and the final NU refinement in C4 symmetry gave a 3.2 Å structure.

For the $TRPV5_{pH6}$ dataset, 4,679 movies were collected. Movies were patch motion corrected with an alignment resolution of 3 Å and Fourier cropped to half the resolution. The micrographs were then run through patch CTF estimation. 740 micrographs with estimated max resolutions below 4 Å were excluded from further processing. The remaining 3939 micrographs were then autopicked using 2D templates generated from a subset of 100 micrographs. 578,132 particles were extracted and binned by a factor of 2 with a box size of 128 pixels and sorted with 2D classification. 158,001 particles remained after 1 round of 2D classification. Ab-initio reconstruction with 3 classes was used to generate the initial structure. One class was taken, and 104,184 particles were extracted in a unbinned box size of 256 pixels. These particles were then subjected to heterogeneous refinement with 3 classes. One class with 57,036 particles was taken to Non-uniform (NU) refinement in C1 symmetry (3.4 Å) and subsequently C4 symmetry (3.2 Å). Global and local CTF refinement

were performed and NU refinement in C4 symmetry gave a 3.0 Å structure. Some heterogeneity remained, so one more round of heterogeneous refinement in C4 symmetry yielded a class with 27,988 particles. The final model was solved by NU-refinement with defocus and global CTF refinements to 3.0 Å resolution in C4 symmetry.

For the $TRPV5_{pH5}$ dataset, 1,663 movies were collected. Movies were patch motion corrected with an alignment resolution of 3 Å and Fourier cropped to half the resolution. The micrographs were then run through patch CTF estimation. 213 micrographs with estimated max resolutions below 5 Å were excluded from further processing. The remaining 1,450 micrographs were then autopicked using 2D templates generated from a subset of 200 micrographs. 221,439 particles were extracted binned by a factor of 4 with a box size of 96 pixels and sorted with 2D classification. 24,329 particles remained after 2 rounds of 2D classification. Particles were reextracted in an unbinned box size of 384 pixels. Ab-initio reconstruction of these particles into 3 classes gave one class with 11,398 particles that was subjected to NU refinement in C1 symmetry (4.9 Å) followed by C4 symmetry (3.7 Å). No heterogeneity was seen and the final model with a resolution of 3.7 Å was used.

For the $TRPV5_{PIP2+pH6}$ dataset, 7,006 movies were collected. Movies were patch motion corrected with an alignment resolution of 3 Å and Fourier cropped to half the resolution. The micrographs were then run through patch CTF estimation. 507 micrographs with estimated max resolutions below 5 Å were excluded from further processing. The remaining 6,499 micrographs were then autopicked using 2D templates generated from a subset of 200 micrographs. 1,536,734 particles were extracted binned by a factor of 4 with a box size of 64 pixels and sorted with 2D classification. 599,459 particles remained after 1 round of 2D classification. These particles were extracted in an unbinned box size of 256 pixels. Ab-initio reconstruction with 1 class was used to generate the initial structure that was subjected to Non-uniform (NU) refinement in C1 symmetry (2.9 Å) followed by C4 symmetry (2.8 Å). Using symmetry expansion and 3D variability clustering analysis, the data was divided into 5 clusters. Two clusters represented the open and closed state of the channel. State1 had 102,424 particles and state2 had 114,598 particles after reverting to their original, non-symmetry expanded state. The other three clusters were intermediate states on the transition between state1 and state2. NU refinement in C4 symmetry yielded structures of $TRPV5_{pH6+PIP2\text{-}state1}$ to 2.8 Å and $TRPV5_{pH6\text{-}state2}$ to 3.0 Å. Heterogeneous refinement with 3 classes yielded 1 class for each state that went to high resolution. The best class for $TRPV5_{pH6+PIP2\text{-}state1}$ contained 63,746 particles and the best class for $TRPV5_{pH6\text{-}state2}$ contained 67,926 particles. For the final models, NU refinement was performed in C4 symmetry on $TRPV5_{pH6+PIP2\text{-}state1}$ and $TRPV5_{pH6\text{-}state2}$, yielding maps with 2.8 Å and 2.9 Å resolution, respectively.

For the $TRPV5_{pH6\text{-}state3}$ dataset, 11,244 movies were collected. Movies were patch motion corrected with an alignment resolution of 3 Å and Fourier cropped to half the resolution. The micrographs were then run through patch CTF estimation. 605 micrographs with estimated max resolutions below 5 Å were excluded from further processing. The remaining 10,639 micrographs were then autopicked using 2D templates generated from a subset of 200 micrographs. 1,772,051 particles were extracted binned by a factor of 4 with a box size of 96 pixels and sorted with 2D classification. 373,133 particles remained after 2 rounds of

2D classification. These particles were extracted in an unbinned box size of 384 pixels. Ab-initio reconstruction with 1 class was used to generate the initial structure that was subjected to Non-uniform (NU) refinement in C1 symmetry (2.9 Å) followed by C4 symmetry (2.6 Å). The particles were then subjected to heterogeneous refinement with 4 classes with C4 symmetry. Only one class went to high resolution with 241,089 particles. This subset of particles was subjected to NU refinement in C4 symmetry (2.5 Å). Using symmetry expansion and 3D variability analysis, it was found that not much movement existed in the channel except for some heterogeneity at the lower gate Trp583 residue. One more round of heterogeneous refinement with 4 classes yielded 3 classes with a stable density for residue Trp583 totaling 172,497 particles and 1 class with the heterogeneous density totaling 68,592 particles. The remainder of the density between these two types of classes was identical. For the final model, NU refinement was performed in C4 symmetry on the classes with stable density, yielding a map with 2.6 Å resolution.

For $TRPV5_{PKA}$, two datasets were used from the same grids with 7,393 and 8,732 movies for dataset 1 and 2 respectively. Movies were patch motion corrected with an alignment resolution of 3 Å and Fourier cropped to half the resolution. The micrographs were then run through patch CTF estimation. 1,053 micrographs from dataset 1 and 2,171 micrographs from dataset 2 with estimated max resolutions below 5 Å were excluded from further processing. The remaining 6,240 and 6,561 micrographs were then separately autopicked using 2D templates generated from subsets of 100 micrographs. 554,184 and 733,430 particles were extracted binned by a factor of 2 with a box size of 128 pixels and sorted with 2D classification. 123,348 and 172,798 particles remained after 1 round of 2D classification in each respective dataset. Particles were then combined and ab-initio reconstruction into 6 classes gave 1 class with 148,299 particles. Homogeneous refinement in C1 symmetry yielded a 4.5 Å structure. Extraction of these particles in an unbinned box size of 256 pixels allowed homogeneous refinement to reach 3.7 Å. However, it was apparent that this sample had some dimers of TRPV5 tetramers. To sort these particles, they were extracted in a larger box size of 416 pixels and 2D classified to efficiently remove these dimers. Homogeneous refinement reached to 3.7 Å. Particles were then taken to heterogenous refinement with 3 classes in C1 symmetry, and the best class with 69,059 particles was taken and NU refinement was performed resulting in a 3.3 Å structure in C4 symmetry. An additional round of heterogenous refinement into 3 classes in C4 symmetry gave 1 class with good density for the channel containing 43,926 particles. NU refinement in C4 symmetry gave a 3.2 Å structure. Global and local CTF refinement followed by one more NU refinement in C4 symmetry gave a 3.1 Å structure. This structure, even in C4 symmetry had extra density inside the ARD skirt of the channel. To investigate, symmetry expansion and 3D variability analysis of 5 component modes was performed. Three of the components showed variability in the ARD skirt, so particles along the axis of this variability when the extra density appears were taken by specifying the coordinate along each mode. From this, 6,016 non-symmetry expanded particles made up the small subset of particles with this density. A final local refinement centered on this density was performed in C1 symmetry, yielding a 4.2 Å structure.

For the $TRPV5_{T709D}$ dataset, 10,011 movies were collected. Movies were patch motion corrected with an alignment resolution of 5 Å and Fourier cropped to half the resolution.

The micrographs were then run through patch CTF estimation. 1,211 micrographs with estimated max resolutions below 5 Å were excluded from further processing. The remaining 8,800 micrographs were then autopicked using 2D templates generated from a subset of 100 micrographs. 2,747,656 particles were extracted binned by a factor of 2 and sorted with 2D classification. 938,370 particles remained after 1 round of 2D classification. Ab-initio reconstruction with 5 classes was performed and resulted in 1 good class to be used as the initial volume for NU refinement in C1 symmetry which gave a 4.3 Å structure. Extraction of the unbinned particles with a box size of 256 and NU refinement yielded a structure with a resolution of 3.1 Å in C1 symmetry, and 3.0 Å in C4 symmetry. Heterogeneous refinement into 5 classes gave 1 class that went to high resolution containing 419,343 particles. Final NU refinement in C4 symmetry yielded a map with 2.8 Å resolution.

For the $TRPV5_{T709D+PIP2}$ dataset, 10,021 movies were collected. Movies were patch motion corrected with an alignment resolution of 5 Å and Fourier cropped to half the resolution. The micrographs were then run through patch CTF estimation. 1,960 micrographs with estimated max resolutions below 5 Å were excluded from further processing. The remaining 8,061 micrographs were then autopicked using 2D templates generated from a subset of 100 micrographs. 1,306,911 particles were extracted binned by a factor of 2 with a box size of 128 pixels and sorted with 2D classification. 342,338 particles remained after 1 round of 2D classification. Ab-initio reconstruction with 5 classes was performed and resulted in 1 good class to be used as the initial volume for heterogeneous refinement in C1 symmetry which gave one good class containing 157,152 particles. Extraction of the unbinned particles with a box size of 256 and NU refinement yielded a structure with a resolution of 3.4 Å in C1 symmetry, and 3.2 Å in C4 symmetry. Global and local CTF refinement improved the resolution to 3.1 Å with NU refinement in C4 symmetry. Symmetry expansion and 3D variability analysis with 5 clusters allowed for sorting of the open state of the channel with bound $PI(4,5)P_2$ containing 30,765 particles. Final NU refinement in C4 symmetry yielded a map with 3.4 Å resolution.

For the $TRPV5_{T709D+CaM}$ dataset, 9,830 movies were collected. Movies were patch motion corrected with an alignment resolution of 3 Å and no Fourier cropping. The micrographs were then run through patch CTF estimation. 1,857 micrographs with estimated max resolutions below 5 Å were excluded from further processing. The remaining 7,972 micrographs were then autopicked using 2D templates generated from a subset of 200 micrographs. 961,168 particles were extracted binned by a factor of 8 with a box size of 72 pixels and sorted with 2D classification. 198,687 particles remained after 1 round of 2D classification. Ab-initio reconstruction with 1 class was performed on these binned particles. Extraction was then performed binned by a factor of 2 with a box size of 288 pixels. NU refinement was performed in C1 symmetry to a resolution of 3.3 Å. Heterogeneous refinement into 6 classes using initial models of the previous model and imported TRPV5 CaM complex from EMDB: 7967 gave 1 class that was capable of reaching high resolution. There was no indication of any additional density belonging to CaM in any of the models. NU refinement in C1 and C4 symmetry yielded 3.2 Å and 3.0 Å maps that were identical. The C4 map was taken as the final model.

Model building—The previously determined full-length rabbit TRPV5 structure (PDB: 6DMR) was used as the starting model and docked into each structure and manually fit and adjusted in COOT (Emsley and Cowtan, 2004) then refined in PHENIX using phenix.real_space_refine with C4 symmetry (Adams et al., 2002). Residues 1–28, 226–229, and 640–730 were excluded from the model because the density was not resolved. The ligand restraint file for $PI(4,5)P_2$ was generated by the eLBOW tool within the PHENIX software package (Moriarty et al., 2009). Models were then aligned and visualized using Pymol and Chimera and ChimeraX (Goddard et al., 2018; Pettersen et al., 2004, 2021; Schrodinger, 2015). Pore radii were measured using HOLE (Smart et al., 1996). Model to map fit was assessed using EMRinger (Barad et al., 2015).

QUANTIFICATION AND STATISTICAL ANALYSIS

Cryo-EM data were processed using cryoSPARC v3.2.0 (Punjani and Fleet, 2021; Punjani et al., 2017, 2020). Cryo-EM structural statistics were analyzed by Phenix (Adams et al., 2002), Molprobity (Chen et al., 2010), EMRinger (Barad et al., 2015) and UCSF Chimera (Pettersen et al., 2004). Standard deviation is used to create error bars in Figures 1A, 4E, and 5J. Two-sample t test was performed in Figure 4E. Statistical details are explained in the figure captions.

Supplementary Material

Refer to Web version on PubMed Central for supplementary material.

ACKNOWLEDGMENTS

We are grateful for the support of Sabine Baxter in managing hybridoma and cell culture at the University of Pennsylvania Perelman School of Medicine Cell Center Services Facility. We thank Dr. Ji-fang Zhang at Thomas Jefferson University for the gift of the rat calmodulin plasmid. We acknowledge the support of the Electron Microscopy Resource Lab and the Beckman Center for Cryo-Electron Microscopy at the University of Pennsylvania Perelman School of Medicine for the use of instruments. We also thank Stefan Steimle for assistance with the Krios microscope operation and data collection. We also acknowledge the use of instruments at the Electron Imaging Center for NanoMachines supported by the NIH (1S10RR23057, 1S10OD018111, and 1U24GM116792), NSF (DBI-1338135), and CNSI at UCLA. Computational resources were in part supported by NIH grant S10OD023592. This work was supported by grants from the NIH (R01GM103899, R01GM129357, and 1R35GM144120 to V.Y.M.-B. and R01GM093290 to T.R.) and by NIH training grant T32GM132039 (to E.C.F.).

REFERENCES

Adams PD, Grosse-Kunstleve RW, Hung LW, Ioerger TR, McCoy AJ, Moriarty NW, Read RJ, Sacchettini JC, Sauter NK, and Terwilliger TC (2002). PHENIX: building new software for automated crystallographic structure determination. Acta Crystallogr. D Biol. Crystallogr 58, 1948–1954. [PubMed: 12393927]

Barad BA, Echols N, Wang RY, Cheng Y, DiMaio F, Adams PD, and Fraser JS (2015). EMRinger: side chain-directed model and map validation for 3D cryo-electron microscopy. Nat. Methods 12, 943–946. [PubMed: 26280328]

Bindels RJ, Hartog A, Abrahamse SL, and Van Os CH (1994). Effects of pH on apical calcium entry and active calcium transport in rabbit cortical collecting system. Am. J. Physiol 266, F620–F627. [PubMed: 8184895]

Cao C, Zakharian E, Borbiro I, and Rohacs T (2013). Interplay between calmodulin and phosphatidylinositol 4,5-bisphosphate in Ca^{2+}-induced inactivation of transient receptor potential vanilloid 6 channels. J. Biol. Chem 288, 5278–5290. [PubMed: 23300090]

Cha SK, Jabbar W, Xie J, and Huang CL (2007). Regulation of TRPV5 single-channel activity by intracellular pH. J. Membr. Biol 220, 79–85. [PubMed: 18004496]

Chen VB, Arendall WB 3rd, Headd JJ, Keedy DA, Immormino RM, Kapral GJ, Murray LW, Richardson JS, and Richardson DC (2010). MolProbity: all-atom structure validation for macromolecular crystallography. Acta Crystallogr. D Biol. Crystallogr 66, 12–21. [PubMed: 20057044]

Dang S, van Goor MK, Asarnow D, Wang Y, Julius D, Cheng Y, and van der Wijst J (2019). Structural insight into TRPV5 channel function and modulation. Proc. Natl. Acad. Sci. U S A 116, 8869–8878. [PubMed: 30975749]

de Groot T, Bindels RJ, and Hoenderop JG (2008). TRPV5: an ingeniously controlled calcium channel. Kidney Int. 74, 1241–1246. [PubMed: 18596722]

de Groot T, Kovalevskaya NV, Verkaart S, Schilderink N, Felici M, van der Hagen EA, Bindels RJ, Vuister GW, and Hoenderop JG (2011). Molecular mechanisms of calmodulin action on TRPV5 and modulation by parathyroid hormone. Mol. Cell Biol 31, 2845–2853. [PubMed: 21576356]

de Groot T, Lee K, Langeslag M, Xi Q, Jalink K, Bindels RJ, and Hoenderop JG (2009). Parathyroid hormone activates TRPV5 via PKA-dependent phosphorylation. J. Am. Soc. Nephrol 20, 1693–1704. [PubMed: 19423690]

Donald JE, Kulp DW, and DeGrado WF (2011). Salt bridges: geometrically specific, designable interactions. Proteins 79, 898–915. [PubMed: 21287621]

Emsley P, and Cowtan K (2004). Coot: model-building tools for molecular graphics. Acta Crystallogr. D Biol. Crystallogr 60, 2126–2132. [PubMed: 15572765]

Fathizadeh A, Senning E, and Elber R (2021). Impact of the protonation state of phosphatidylinositol 4,5-bisphosphate (PIP_2) on the binding kinetics and thermodynamics to transient receptor potential vanilloid (TRPV5): a milestoning study. J. Phys. Chem. B 125, 9547–9556. [PubMed: 34396776]

Fluck EC, Pumroy RA, and Moiseenkova-Bell VY (2021). Production and purification of TRPV2 and TRPV5 for structural and functional studies. Methods Enzymol. 653, 49–74. [PubMed: 34099181]

Frick KK, and Bushinsky DA (2003). Molecular mechanisms of primary hypercalciuria. J. Am. Soc. Nephrol 14, 1082–1095. [PubMed: 12660344]

Goddard TD, Huang CC, Meng EC, Pettersen EF, Couch GS, Morris JH, and Ferrin TE (2018). UCSF ChimeraX: meeting modern challenges in visualization and analysis. Protein Sci. 27, 14–25. [PubMed: 28710774]

Grinkova YV, Denisov IG, and Sligar SG (2010). Engineering extended membrane scaffold proteins for self-assembly of soluble nanoscale lipid bilayers. Protein Eng. Des. Sel 23, 843–848. [PubMed: 20817758]

Hodges RS, Heaton RJ, Parker JM, Molday L, and Molday RS (1988). Antigen-antibody interaction. Synthetic peptides define linear antigenic determinants recognized by monoclonal antibodies directed to the cytoplasmic carboxyl terminus of rhodopsin. J. Biol. Chem 263, 11768–11775. [PubMed: 2457026]

Hoenderop JG, Nilius B, and Bindels RJ (2002). Molecular mechanism of active Ca^{2+} reabsorption in the distal nephron. Annu. Rev. Physiol 64, 529–549. [PubMed: 11826278]

Hoenderop JG, Nilius B, and Bindels RJ (2005). Calcium absorption across epithelia. Physiol. Rev 85, 373–422. [PubMed: 15618484]

Hoenderop JG, van der Kemp AW, Hartog A, van Os CH, Willems PH, and Bindels RJ (1999). The epithelial calcium channel, ECaC, is activated by hyperpolarization and regulated by cytosolic calcium. Biochem. Biophys. Res. Commun 261, 488–492. [PubMed: 10425212]

Hoenderop JG, van Leeuwen JP, van der Eerden BC, Kersten FF, van der Kemp AW, Merillat AM, Waarsing JH, Rossier BC, Vallon V, Hummler E, et al. (2003). Renal Ca^{2+} wasting, hyperabsorption, and reduced bone thickness in mice lacking TRPV5. J. Clin. Invest 112, 1906–1914. [PubMed: 14679186]

Hughes TE, Del Rosario JS, Kapoor A, Yazici AT, Yudin Y, Fluck EC 3rd, Filizola M, Rohacs T, and Moiseenkova-Bell VY (2019). Structure-based characterization of novel TRPV5 inhibitors. Elife 8, e49572. [PubMed: 31647410]

Hughes TET, Lodowski DT, Huynh KW, Yazici A, Del Rosario J, Kapoor A, Basak S, Samanta A, Han X, Chakrapani S, et al. (2018a). Structural basis of TRPV5 channel inhibition by econazole revealed by cryo-EM. Nat. Struct. Mol. Biol 25, 53–60. [PubMed: 29323279]

Hughes TET, Pumroy RA, Yazici AT, Kasimova MA, Fluck EC, Huynh KW, Samanta A, Molugu SK, Zhou ZH, Carnevale V, et al. (2018b). Structural insights on TRPV5 gating by endogenous modulators. Nat. Commun 9, 4198. [PubMed: 30305626]

Lee J, Cha SK, Sun TJ, and Huang CL (2005). PIP_2 activates TRPV5 and releases its inhibition by intracellular Mg^{2+}. J. Gen. Physiol 126, 439–451. [PubMed: 16230466]

Moiseenkova-Bell VY, Stanciu LA, Serysheva II, Tobe BJ, and Wensel TG (2008). Structure of TRPV1 channel revealed by electron cryomicroscopy. Proc. Natl. Acad. Sci. U S A 105, 7451–7455. [PubMed: 18490661]

Moriarty NW, Grosse-Kunstleve RW, and Adams PD (2009). Electronic Ligand Builder and Optimization Workbench (eLBOW): a tool for ligand coordinate and restraint generation. Acta Crystallogr. D Biol. Crystallogr 65, 1074–1080. [PubMed: 19770504]

Na T, and Peng JB (2014). TRPV5: a Ca^{2+} channel for the fine-tuning of Ca^{2+} reabsorption. Handb. Exp. Pharmacol 222, 321–357. [PubMed: 24756712]

Niemeyer BA, Bergs C, Wissenbach U, Flockerzi V, and Trost C (2001). Competitive regulation of CaT-like-mediated Ca^{2+} entry by protein kinase C and calmodulin. Proc. Natl. Acad. Sci. U S A 98, 3600–3605. [PubMed: 11248124]

Nijenhuis T, Renkema KY, Hoenderop JG, and Bindels RJ (2006). Acid-base status determines the renal expression of Ca^{2+} and Mg^{2+} transport proteins. J. Am. Soc. Nephrol 17, 617–626. [PubMed: 16421227]

Oddsson A, Sulem P, Helgason H, Edvardsson VO, Thorleifsson G, Sveinbjornsson G, Haraldsdottir E, Eyjolfsson GI, Sigurdardottir O, Olafsson I, et al. (2015). Common and rare variants associated with kidney stones and biochemical traits. Nat. Commun 6, 7975. [PubMed: 26272126]

Peng JB (2011). TRPV5 and TRPV6 in transcellular Ca^{2+} transport: regulation, gene duplication, and polymorphisms in African populations. Adv. Exp. Med. Biol 704, 239–275. [PubMed: 21290300]

Peng JB, Chen XZ, Berger UV, Vassilev PM, Tsukaguchi H, Brown EM, and Hediger MA (1999). Molecular cloning and characterization of a channel-like transporter mediating intestinal calcium absorption. J. Biol. Chem 274, 22739–22746. [PubMed: 10428857]

Pettersen EF, Goddard TD, Huang CC, Couch GS, Greenblatt DM, Meng EC, and Ferrin TE (2004). UCSF Chimera–a visualization system for exploratory research and analysis. J. Comput. Chem 25, 1605–1612. [PubMed: 15264254]

Pettersen EF, Goddard TD, Huang CC, Meng EC, Couch GS, Croll TI, Morris JH, and Ferrin TE (2021). UCSF ChimeraX: structure visualization for researchers, educators, and developers. Protein Sci. 30, 70–82. [PubMed: 32881101]

Punjani A, and Fleet DJ (2021). 3D variability analysis: resolving continuous flexibility and discrete heterogeneity from single particle cryo-EM. J. Struct. Biol 213, 107702. [PubMed: 33582281]

Punjani A, Rubinstein JL, Fleet DJ, and Brubaker MA (2017). cryo-SPARC: algorithms for rapid unsupervised cryo-EM structure determination. Nat. Methods 14, 290–296. [PubMed: 28165473]

Punjani A, Zhang H, and Fleet DJ (2020). Non-uniform refinement: adaptive regularization improves single-particle cryo-EM reconstruction. Nat. Methods 17, 1214–1221. [PubMed: 33257830]

Rohacs T (2014). Phosphoinositide regulation of TRP channels. Handb. Exp. Pharmacol 233, 1143–1176.

Rohacs T, Lopes CM, Michailidis I, and Logothetis DE (2005). $PI(4,5)P_2$ regulates the activation and desensitization of TRPM8 channels through the TRP domain. Nat. Neurosci 8, 626–634. [PubMed: 15852009]

Schrodinger LLC (2015). The PyMOL Molecular Graphics System, Version 2.3.

Singh AK, McGoldrick LL, Twomey EC, and Sobolevsky AI (2018). Mechanism of calmodulin inactivation of the calcium-selective TRP channel TRPV6. Sci. Adv 4, eaau6088. [PubMed: 30116787]

Smart OS, Neduvelil JG, Wang X, Wallace BA, and Sansom MS (1996). HOLE: a program for the analysis of the pore dimensions of ion channel structural models. J. Mol. Graph 14, 354–360. [PubMed: 9195488]

Suh BC, and Hille B (2008). PIP2 is a necessary cofactor for ion channel function: how and why? Annu. Rev. Biophys 37, 175–195. [PubMed: 18573078]

van Abel M, Hoenderop JG, van der Kemp AW, Friedlaender MM, van Leeuwen JP, and Bindels RJ (2005). Coordinated control of renal Ca^{2+} transport proteins by parathyroid hormone. Kidney Int. 68, 1708–1721. [PubMed: 16164647]

van de Graaf SF, Bindels RJ, and Hoenderop JG (2007). Physiology of epithelial Ca^{2+} and Mg^{2+} transport. Rev. Physiol. Biochem. Pharmacol 158, 77–160. [PubMed: 17729442]

van der Wijst J, van Goor MK, Schreuder MF, and Hoenderop JG (2019). TRPV5 in renal tubular calcium handling and its potential relevance for nephrolithiasis. Kidney Int. 96, 1283–1291. [PubMed: 31471161]

van Goor MKC, Hoenderop JGJ, and van der Wijst J (2017). TRP channels in calcium homeostasis: from hormonal control to structure-function relationship of TRPV5 and TRPV6. Biochim. Biophys. Acta Mol. Cell Res 1864, 883–893. [PubMed: 27913205]

Velisetty P, Borbiro I, Kasimova MA, Liu L, Badheka D, Carnevale V, and Rohacs T (2016). A molecular determinant of phosphoinositide affinity in mammalian TRPV channels. Sci. Rep 6, 27652. [PubMed: 27291418]

Wagner CA, and Mohebbi N (2010). Urinary pH and stone formation. J. Nephrol 23 (Suppl 16), S165–S169. [PubMed: 21170875]

Wang L, Holmes RP, and Peng JB (2017). The L530R variation associated with recurrent kidney stones impairs the structure and function of TRPV5. Biochem. Biophys. Res. Commun 492, 362–367. [PubMed: 28847730]

Yeh BI, Kim YK, Jabbar W, and Huang CL (2005). Conformational changes of pore helix coupled to gating of TRPV5 by protons. EMBO J. 24, 3224–3234. [PubMed: 16121193]

Yeh BI, Sun TJ, Lee JZ, Chen HH, and Huang CL (2003). Mechanism and molecular determinant for regulation of rabbit transient receptor potential type 5 (TRPV5) channel by extracellular pH. J. Biol. Chem 278, 51044–51052. [PubMed: 14525991]

Yeh BI, Yoon J, and Huang CL (2006). On the role of pore helix in regulation of TRPV5 by extracellular protons. J. Membr. Biol 212, 191–198. [PubMed: 17334836]

Zhang M, Meng XY, Cui M, Pascal JM, Logothetis DE, and Zhang JF (2014). Selective phosphorylation modulates the PIP_2 sensitivity of the CaM-SK channel complex. Nat. Chem. Biol 10 (9), 753–759. [PubMed: 25108821]

Zhou Y, and Greka A (2016). Calcium-permeable ion channels in the kidney. Am. J. Physiol. Ren. Physiol 310, F1157–F1167.

Highlights

- The TRPV5 ion channel is essential for calcium homeostasis
- Acidic pH inhibits TRPV5 through conformational change and loss of $PI(4,5)P_2$
- PKA phosphorylates TRPV5 and prevents CaM inactivation

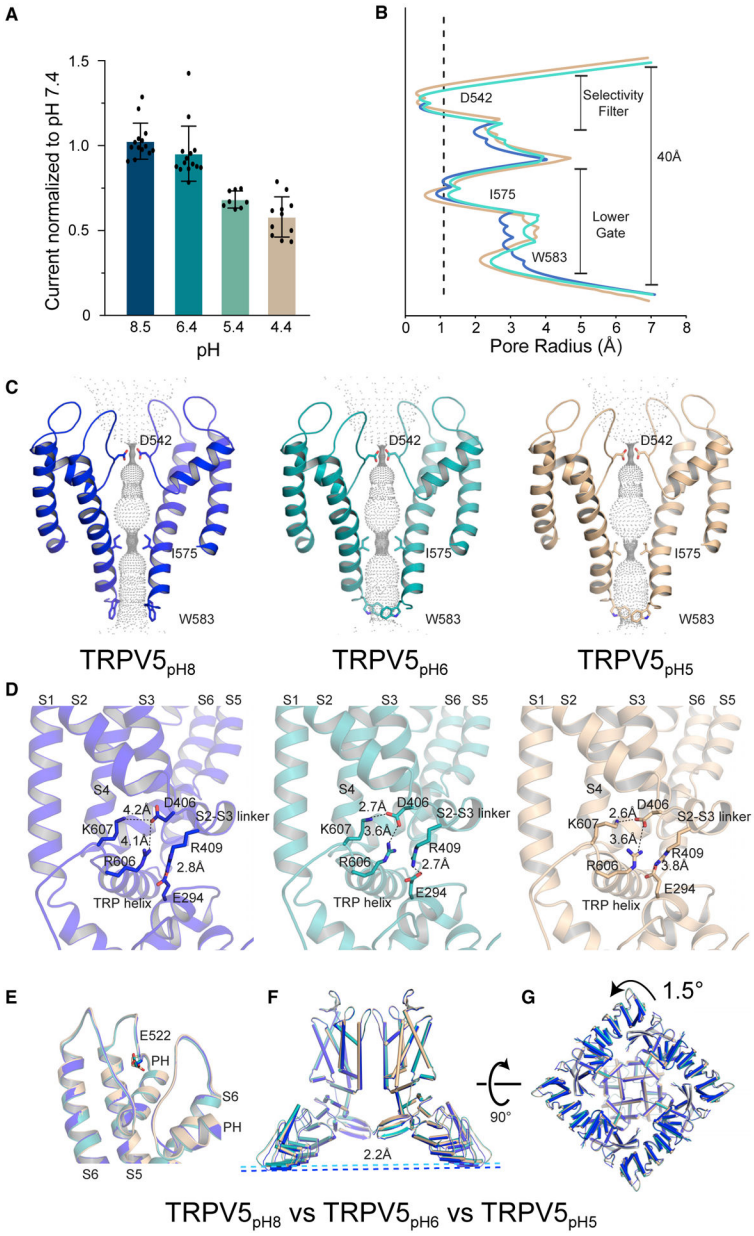

Figure 1. TRPV5 structures and function in high and low pH

(A) TEVC data showing TRPV5 channel activity in *Xenopus* oocytes under various pH states. Measurement of monovalent currents through TRPV5 were performed as described in the STAR Methods. Currents were normalized to pH 7.4 values for each oocyte and plotted as mean ± SD and as scatterplots.

(B) Pore diagram plotting pore radius of $TRPV5_{pH8}$ (blue), $TRPV5_{pH6}$ (teal), and $TRPV5_{pH5}$ (wheat) as a function of distance along the ion-conducting pore.

(C) Pore profiles of $TRPV5_{pH8}$ (blue), $TRPV5_{pH6}$ (teal), and $TRPV5_{pH5}$ (wheat) highlighting constriction residues D542, I575, and W583.

(D) Residues around the intracellular pH sensor K607 are highlighted, with distances labeled between residues involved in salt bridge formation.

(E) Extracellular pH sensor E522.
(F) Comparison between $TRPV5_{pH6}$ (teal) and $TRPV5_{pH5}$ (wheat) in reference to $TRPV5_{pH8}$ (blue) showing the positions of the ARD.
(G) Comparison between $TRPV5_{pH6}$ (teal) and $TRPV5_{pH5}$ (wheat) in reference to $TRPV5_{pH8}$ (blue) showing the rotation of the ARD. See also Figures S1–S4.

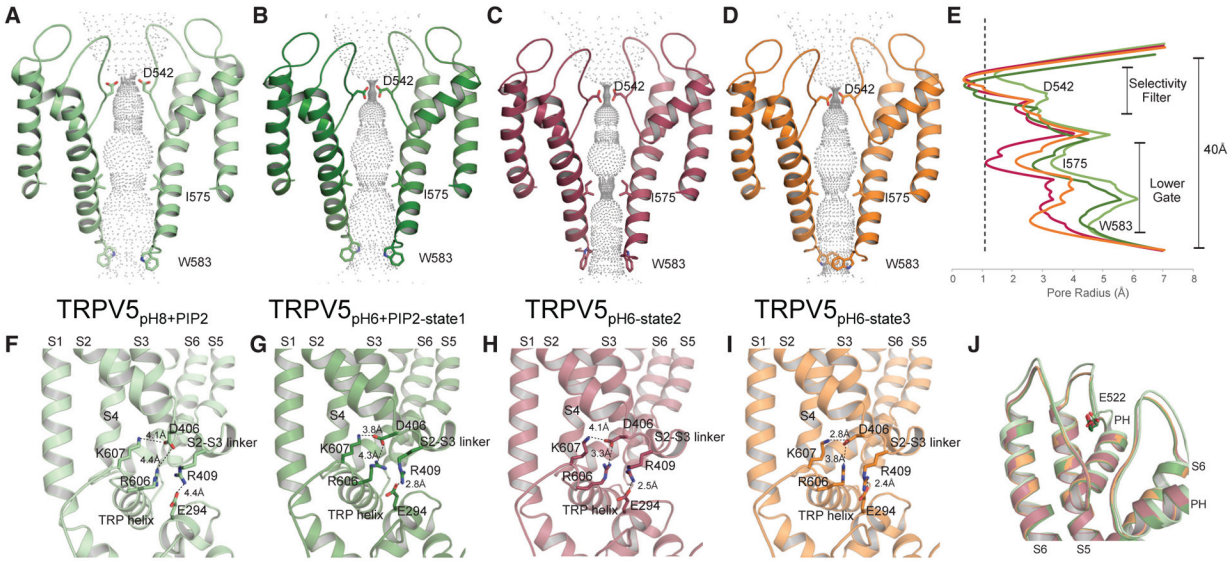

Figure 2. Interplay between pH and PI(4,5)P_2 on the TRPV5 structure

(A–D) Pore profiles of (A) $TRPV5_{pH8+PIP2}$ (pale green), (B) $TRPV5_{pH6+PIP2\text{-}state1}$ (dark green), (C) $TRPV5_{pH6\text{-}state2}$ (dark red), and (D) $TRPV5_{pH6\text{-}state3}$ (orange).

(E) The pore diagram plotted along the ion-conducting pore.

(F–I) Residues around the intracellular pH sensor K607 are highlighted, with distances labeled between residues involved in salt-bridge formation.

(J) Extracellular pH sensor E522. See also Figures S3–S5.

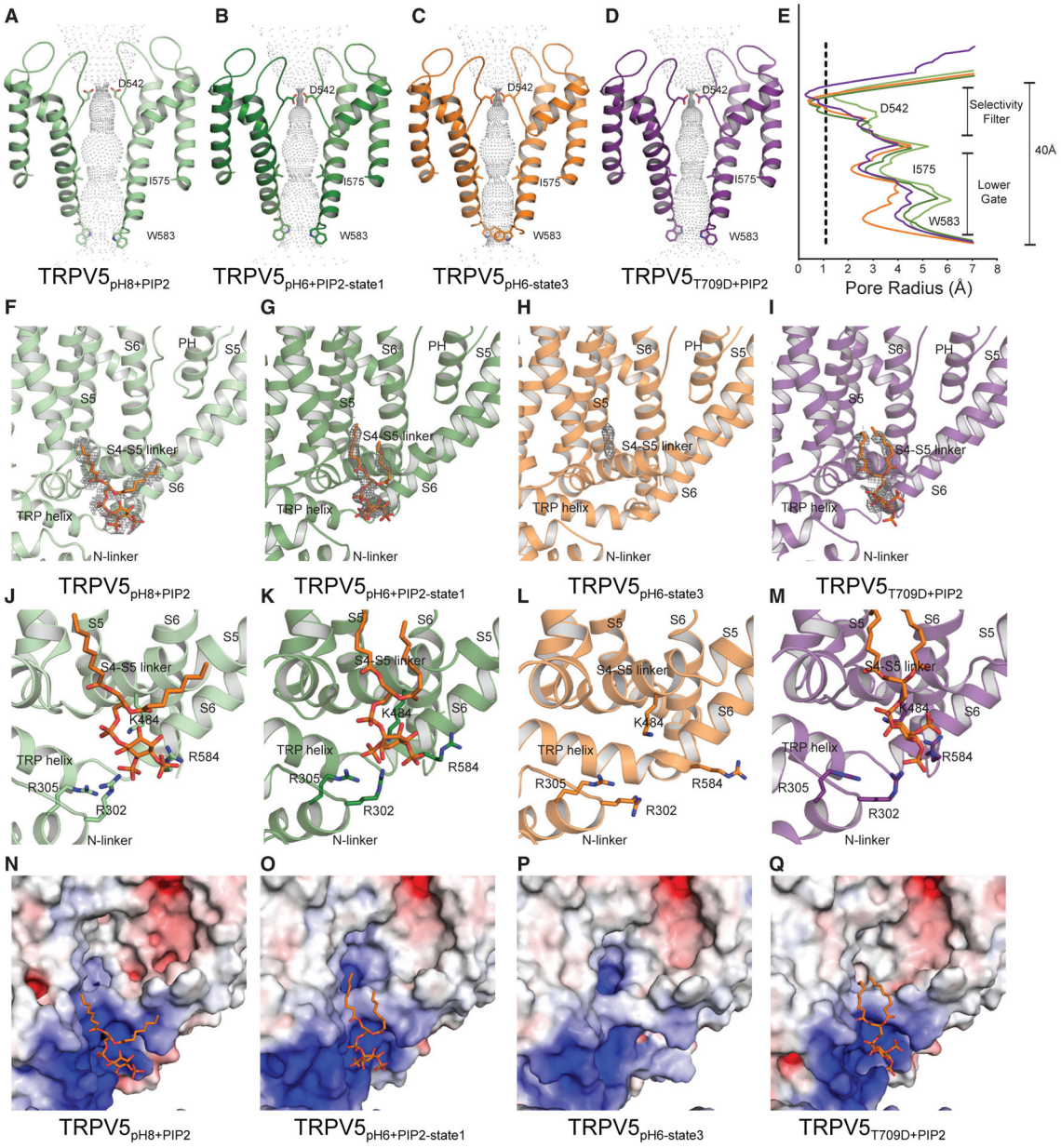

Figure 3. PI(4,5)P_2 binding site of TRPV5 and effect on channel gating

(A–E) View of the pore profiles of (A) TRPV5$_{pH8+PIP2}$ (pale green), (B) TRPV5$_{pH6+PIP2-state1}$ (dark green), (C) TRPV5$_{pH6-state3}$ (orange), and (D) TRPV5$_{T709D+PIP2}$ (purple), highlighting constriction residues D542, I575, and W583, along with (E) the pore diagram plotting pore radius as a function of distance along the ion-conducting pore.

(F–I) PI(4,5)P_2 binding sites of each model with overlaid density contoured at σ = 3.5.

(J–M) Close ups of PI(4,5)P_2 binding sites with the positions of R302, R305, K484, and R584.

(N–Q) Calculated electrostatic potential of PI(4,5)P_2 binding sites.

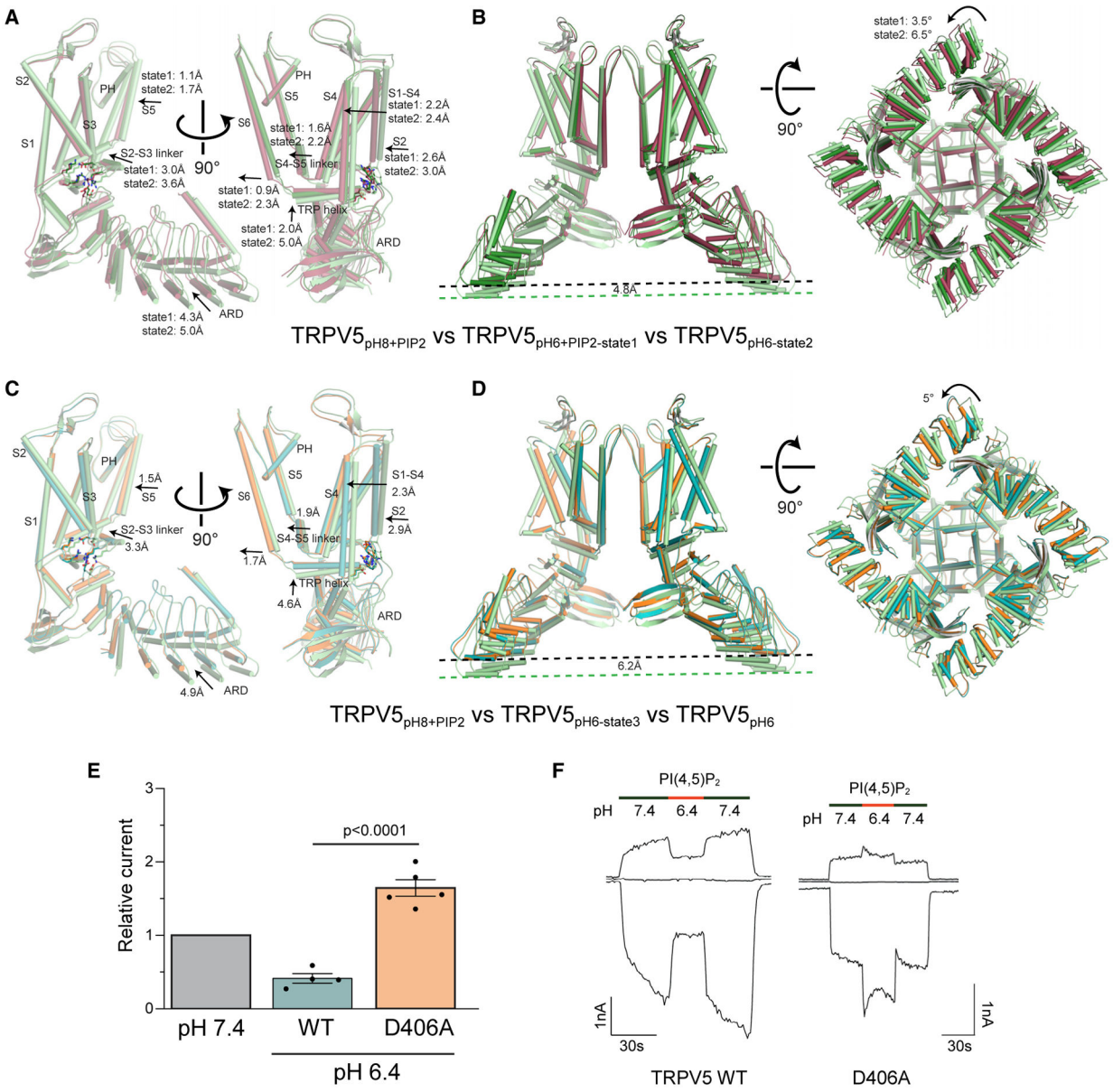

Figure 4. Conformational changes in TRPV5 with pH and PI(4,5)P$_2$

(A) Overlay of monomers in two views and movements of TRPV5$_{pH6+PIP2-state1}$ (dark green) and TRPV5$_{pH6-state2}$ (dark red) in reference to TRPV5$_{pH8+PIP2}$ (pale green).

(B) Comparison of TRPV5$_{pH6+PIP2-state1}$ (dark green) and TRPV5$_{pH6-state2}$ (dark red) in reference to TRPV5$_{pH8+PIP2}$ (pale green) showing the positions and rotation of the ARD.

(C) Overlay of monomers in two views and movements of TRPV5$_{pH6-state3}$ (orange) and TRPV5$_{pH6}$ (teal) in reference to TRPV5$_{pH8+PIP2}$ (pale green).

(D) Comparison of TRPV5$_{pH6-state3}$ (orange) and TRPV5$_{pH6}$ (teal) in reference to TRPV5$_{pH8+PIP2}$ (pale green) showing the positions and rotations of the ARD.

(E) Data summary of TRPV5 excised inside-out patch-clamp experiments (see STAR Methods). Current values (−100 mV) at pH 6.4 are normalized to pH 7.4 for wild-type (WT) TRPV5 and for the D406A mutant. First column visually shows the reference point

(pH 7.4), and two-sample t test was used to compare WT and D406A data points. Data were plotted as the mean ± SD.

(F) Representative traces show monovalent inward currents at −100, 0, and 100 mV. Currents were evoked after rundown by application of 25 μM diC_8 PI(4,5)P_2, and the pH of the solution was alternated between pH 7.4 and pH 6.4.

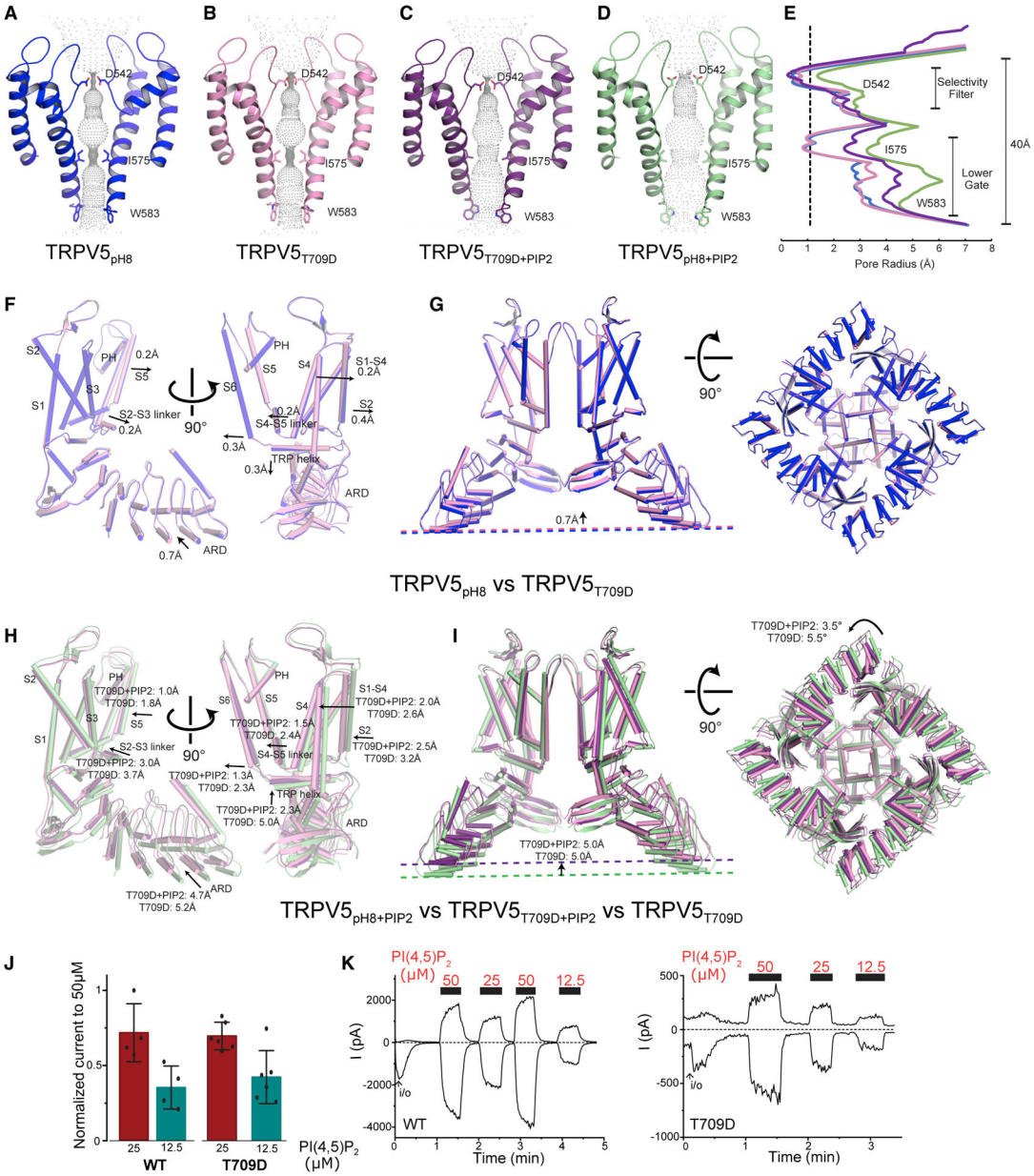

Figure 5. TRPV5 in a phosphorylated state interacts with PI(4,5)P_2

(A–E) Pore profiles of (A) $TRPV5_{pH8}$ (blue), (B) $TRPV5_{T709D}$ (pink), (C) $TRPV5_{T709D+PIP2}$ (purple), and (D) $TRPV5_{pH8+PIP2}$ (pale green) highlighting constriction residues D542, I575, and W583, along with (E) the pore diagram plotting pore radius as a function of distance along the ion-conducting pore.

(F) Overlay of monomers in two views and movement of $TRPV5_{T709D}$ (pink) in reference to $TRPV5_{pH8}$ (blue).

(G) Comparison of $TRPV5_{T709D}$ (pink) in reference to $TRPV5_{pH8}$ (blue) showing the position, but lack of rotation, of the ARD.

(H) Overlay of monomers in two views and movements of $TRPV5_{T709D}$ (pink) and $TRPV5_{T709D+PIP2}$ (purple) in reference to $TRPV5_{pH8+PIP2}$ (pale green).

(I) Comparison of $TRPV5_{T709D}$ (pink) and $TRPV5_{T709D+PIP2}$ (purple) in reference to $TRPV5_{pH8+PIP2}$ (pale green) showing the positions and rotations of the ARD.
(J) Excised inside-out patch-clamp experiments from *Xenopus* oocytes expressing either WT TRPV5 or T709D mutant TRPV5 under different concentrations of $PI(4,5)P_2$. Currents at −100 mV were normalized to 50 μM $PI(4,5)P_2$ for each patch and plotted as the mean ± SD and as scatterplots on the bar graph.
(K) Representative traces for excised patch experiments. Measurements of monovalent TRPV5 currents were performed as described under STAR Methods. Top traces show currents at 100 mV, bottom traces at −100 mV; dashed lines show zero current. The establishment of the inside-out configuration (i/o) is indicated by the arrows. Different concentrations of diC_8 $PI(4,5)P_2$ were applied after current rundown, as indicated by the thick horizontal lines. See also Figures S3, S6, and S7.

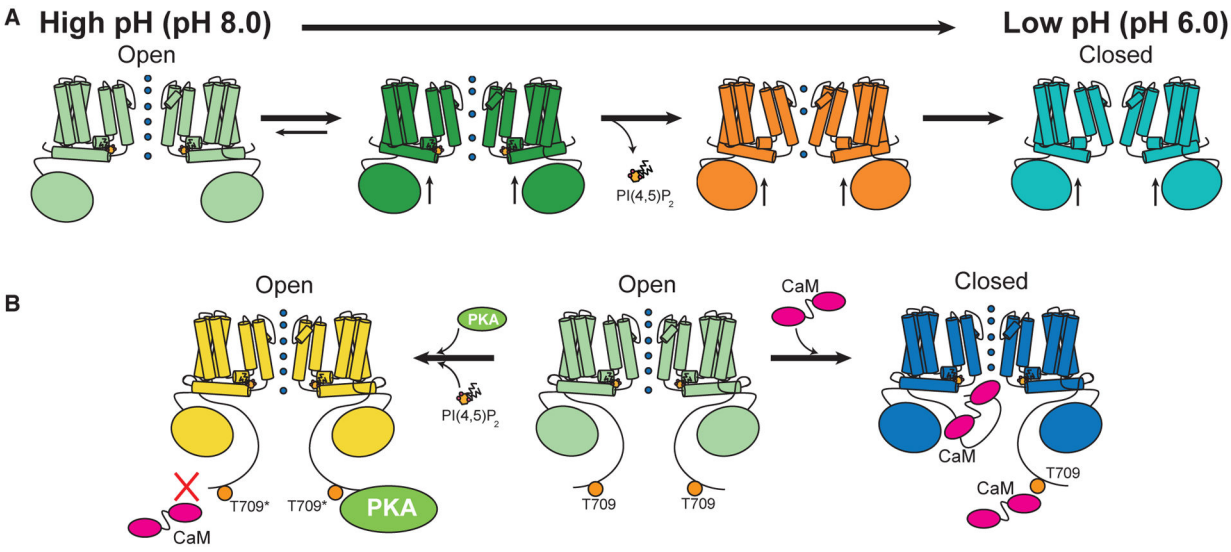

Figure 6. Proposed mechanisms of TRPV5 modulation by pH and PKA

(A) The mechanism of TRPV5 closing with low pH.

(B) The mechanism of inactivation by CaM and activation by PKA.

KEY RESOURCES TABLE

REAGENT or RESOURCE	SOURCE	IDENTIFIER
Antibodies		
1D4 primary antibody	(Hodges et al., 1988)	N/A
Bacterial and virus strains		
XL10-Gold	Agilent	Cat # 200315
BL21(DE3)	Invitrogen	Cat# 44–0048
Chemicals, peptides, and recombinant proteins		
Collagenase	Sigma	Cat# C9891–1G
DpnI restriction enzyme	New England Biolabs	Cat# R0176S
SD-Leu Media	MP Biomedicals	Cat# 4811075
Glycerol	Fisher BioReagents	Cat# BP229–4
Protease inhibitor cocktail	Sigma	Cat# P8215
CnBr-activated sepharose beads	Cytiva	Cat# 17043001
1D4 peptide	Genscript	N/A
Lauryl Maltose Neopentyl Glycol (LMNG)	Anatrace	Cat# NG310
Decyl Maltose Neopentyl Glycol (DMNG)	Anatrace	Cat# NG322
TCEP	Pierce	Cat# PG82090
Soy polar lipids	Avanti	Cat # 541602C
MSP2N2	(Grinkova et al., 2010)	Addgene #29520
Bio-Beads SM-2 Absorbent media	BioRad	Cat# 152–8920
diC8-PI(4,5)P_2	Cayman	Cat # 64910
diC8-PI(4,5)P_2	Echelon Biosciences	Cat# P-4508
cAMP-dependent Protein Kinase (PKA), catalytic subunit	New England Biolabs	Cat# P6000S
Critical commercial assays		
mMessage mMachine T7 kit	Thermo Fisher	Cat# AM1344
Quikchange XL mutagenesis kit	Agilent Genomics	Cat# 200516
Phusion Master Mix	Thermo Scientific	Cat# F-531S
Alkali-Cation Yeast Transformation Kit	MP Biomedicals	Cat# 2200200
Universal Kinase Assay kit	Biovision	Cat# K212–100
Deposited data		
$TRPV5_{pH8}$	This paper	EMDB: 25716 PDB: 7T6J
$TRPV5_{pH6}$	This paper	EMDB: 25717 PDB: 7T6K
$TRPV5_{pH5}$	This paper	EMDB: 25718 PDB: 7T6L
$TRPV5_{pH6+PIP2\text{-}state1}$	This paper	EMDB: 25719 PDB: 7T6M
$TRPV5_{pH6\text{-}state2}$	This paper	EMDB: 25720 PDB: 7T6N
$TRPV5_{pH6\text{-}state3}$	This paper	EMDB: 25721 PDB: 7T6O
$TRPV5_{PKA}$	This paper	EMDB: 25722

REAGENT or RESOURCE	SOURCE	IDENTIFIER
$TRPV5_{T709D}$	This paper	EMDB: 25723 PDB: 7T6P
$TRPV5_{T709D+PIP2}$	This paper	EMDB: 25724 PDB: 7T6Q
$TRPV5_{T709D+CaM}$	This paper	EMDB: 25725 PDB: 7T6R
$TRPV5_{pH8+PIP2}$	(Hughes et al., 2018b)	EMDB: 7966 PDB: 6DMU
Experimental models: Organisms/strains		
Saccharomyces cerevisiae BJ5457	ATCC	208282
Xenopus laevis	Xenopus Express	Cat# LB-XL-FM
Oligonucleotides		
TRPV5 T709D forward primer CCTTCGTCGAAACGACTTGGGACATTGAATCTTGG	This paper	N/A
TRPV5 T709D reverse primer CCAAGATTCAAGTGTCCCAATCTGTTTCGACGAAGG	This paper	N/A
Recombinant DNA		
YepM rabbit TRPV5 plasmid	(Hughes et al., 2018a; Moiseenkova-Bell et al., 2008)	N/A
YepM rabbit TRPV5 T709D plasmid	This paper	N/A
pGEMSH rabbit TRPV5 plasmid	(Hughes et al., 2018a)	N/A
pET28b rat calmodulin plasmid	(Zhang et al., 2014)	N/A
Software and algorithms		
pCLAMP	Molecular Devices	https://www.moleculardevices.com/products/axon-patch-clamp-system/acquisition-andanalysis-software/pclamp-software-suite
cryoSPARC v3.2.0	(Punjani and Fleet, 2021; Punjani et al., 2017, 2020)	https://cryosparc.com/
Coot	(Emsley and Cowtan, 2004)	https://www2.mrc-lmb.cam.ac.uk/personal/pemsley/coot/
Phenix 1.18.2–3874	(Adams et al., 2002)	https://phenix-online.org/documentation/index.html
eLBOW	(Moriarty et al., 2009)	https://phenix-online.org/documentation/reference/elbow_gui.html
Molprobity	(Chen et al., 2010)	http://molprobity.biochem.duke.edu/
EMRinger	(Barad et al., 2015)	https://github.com/fraser-lab/EMRinger
HOLE	(Smart et al., 1996)	http://www.holeprogram.org/
PyMOL	(Schrodinger, 2015)	https://pymol.org/2/
Chimera	(Pettersen et al., 2004)	https://www.cgl.ucsf.edu/chimera/
ChimeraX	(Goddard et al., 2018; Pettersen et al., 2021)	https://www.cgl.ucsf.edu/chimerax/
Other		
Oasis PGA Absorbable Suture	Med Vet International	Cat# MVJ397

Cell Rep. Author manuscript; available in PMC 2022 May 10.

Table 1.

Refinement statistics for TRPV5 structures

	$TRPV5_{pH8}$ (EMDB: 25716, PDB: 7T6J)	**$TRPV5_{pH6}$ (EMDB: 25717, PDB: 7T6K)**	**$TRPV5_{pH5}$ (EMDB: 25718, PDB: 7T6L)**	**$TRPV5_{pH6+PIP2-state1}$ (EMDB: 25719, PDB: 7T6M)**	**$TRPV5_{pH6-state2}$ (EMDB: 25720, PDB: 7T6N)**	**$TRPV5_{pH6-state3}$ (EMDB: 25721, PDB: 7T6O)**	**$TRPV5_{PKA}$ (EMDB: 25722)**	**$TRPV5_{T709D}$ (EMDB: 25723, PDB: 7T6P)**	**$TRPV5_{T709D+PIP2}$ (EMDB: 25724, PDB: 7T6Q)**	**$TRPV5_{T709D+CaM}$ (EMDB: 25725, PDB: 7T6R)**
Data collection and processing										
Magnification	105,000×	81,000×	105,000×	81,000×		105,000×	130,000×	81,000×	81,000×	105,000×
Detector mode	super-resolution	super-resolution	super-resolution	super-resolution		super-resolution	super-resolution	super-resolution	super-resolution	super-resolution
Voltage (kV)	300	300	300	300		300	300	300	300	300
Pixel size (Å)	0.83	1.06	0.83	1.06		0.83	1.07	1.06	1.06	0.83
Total extracted particles (no.)	242,844	578,132	221,439	1,536,734		1,772,051	1,287,614	2,747,656	1,306,911	961,168
Refined particles (no.)	111,116	158,001	24,329	599,459		373,133	296,146	938,370	342,338	198,281
Final particles (no.)	54,415	27,988	11,398	63,746	67,926	172,497	6,016	419,343	30,765	108,153
Symmetry	C4	C4	C4	C4	C4	C4	C1	C4	C4	C4
Map sharpening factor ($Å^2$)	122	82	89	92	92	85	16	110	86	108
Map resolution threshold (Å)	3.2	3.0	3.7	2.8	2.9	2.6	4.2	2.8	3.4	3.0
FSC threshold	0.143	0.143	0.143	0.143	0.143	0.143	0.143	0.143	0.143	0.143
Model refinement										
Resolution cutoff (Å)	3.16	3.00	3.70	2.80	2.90	2.60	-	2.80	3.40	3.00
Model composition										
Non-hydrogen atoms	19,412	19,412	19,412	19,600	19,412	19,412	-	19,412	19,600	19,412
Protein residues	2,424	2,424	2,424	2,424	2,424	2,424	-	2,424	2,424	2,424
Ligands	-	-	-	PIO, 4	-	-	-	-	PIO, 4	-

	$TRPV5_{pH8}$ (EMDB: 25716, PDB: 7T6J)	**$TRPV5_{pH6}$ (EMDB: 25717, PDB: 7T6K)**	**$TRPV5_{pH5}$ (EMDB: 25718, PDB: 7T6L)**	**$TRPV5_{pH6+PIP2-state1}$ (EMDB: 25719, PDB: 7T6M)**	**$TRPV5_{pH6-state2}$ (EMDB: 25720, PDB: 7T6N)**	**$TRPV5_{pH6-state3}$ (EMDB: 25721, PDB: 7T6O)**	**$TRPV5_{PKA}$ (EMDB: 25722)**	**$TRPV5_{T709D}$ (EMDB: 25723, PDB: 7T6P)**	**$TRPV5_{T709D+PIP2}$ (EMDB: 25724, PDB: 7T6Q)**	**$TRPV5_{T709D+CaM}$ (EMDB: 25725, PDB: 7T6R)**
Root-mean-square deviations										
Bond lengths (Å)	0.005	0.005	0.007	0.006	0.007	0.004	-	0.005	0.006	0.005
Bond angles (°)	1.093	1.050	1.179	1.080	1.076	0.793	-	1.127	1.294	1.072
Validation										
MolProbity score	1.38	1.33	1.62	1.10	1.38	1.04	-	1.43	1.52	1.46
Clashscore	3.83	3.34	5.37	3.12	3.98	2.57	-	3.65	4.88	3.44
Poor rotamers (%)	0.05	0.05	0.00	0.00	0.19	0.00	-	0.00	0.00	0.00
CαBLAM outliers (%)	1.63	1.51	1.38	1.84	0.54	0.50	-	3.34	2.17	2.22
EMRinger score	2.58	3.50	1.57	3.89	3.52	3.82	-	2.86	2.18	3.26
Ramachandran plot										
Favored (%)	96.68	96.72	95.18	98.26	96.80	98.67	-	96.01	96.05	95.35
Allowed (%)	3.16	3.28	4.82	1.74	3.20	1.33	-	3.99	3.95	4.85
Disallowed (%)	0.17	0.00	0.00	0.00	0.00	0.00	-	0.00	0.00	0.00